ACCEPTED VERSION

Jingjing Ye, Paul R. Medwell, Konstantin Kleinheinz, Michael J. Evans, Bassam B. Dally, Heinz G. Pitsch

Structural differences of ethanol and DME jet flames in a hot diluted coflow

Published at: http://dx.doi.org/10.1016/j.combustflame.2018.02.025

http://hdl.handle.net/2440/114089

Structural differences of ethanol and DME jet flames in a hot diluted coflow

Jingjing Ye[a,*], Paul R. Medwell[a], Konstantin Kleinheinz[b], Michael J. Evans[a], Bassam B. Dally[a], Heinz G. Pitsch[b]

[a]*School of Mechanical Engineering, The University of Adelaide, South Australia 5005, Australia*
[b]*Institute for Combustion Technology, RWTH Aachen University, Aachen 52056, Germany*

Abstract

This study compares the flame structure of ethanol and dimethyl ether (DME) in a hot and diluted oxidiser experimentally and computationally. Experiments were conducted on a Jet in Hot Coflow (JHC) burner, with the fuel jet issuing into a 1250-K coflow at three oxygen levels. Planar measurements using OH-LIF, CH_2O-LIF, and Rayleigh scattering images reveal that the overall spatial distribution and evolution of OH, CH_2O, and temperature were quite similar for the two fuels. For both the ethanol and the DME flames, a transitional flame structure occurred as the coflow oxygen level increased from 3% to 9%. This indicates that the flames shift away from the MILD combustion regime. Reaction flux analyses of ethanol and DME were performed with the OPPDIF code, and ethane (C_2H_6) was also included in the analyses for comparison. These analyses reveal that the H_2/O_2 pathways are very important for both ethanol and DME in the 3% O_2 cases. In contrast, the importance of fuel-specific reactions overtakes that of H_2/O_2 reactions when fuels are burnt in the cold air or in the vitiated oxidant stream with 9% O_2. Unsteady laminar flamelet analyses were also performed to investigate the ignition processes and help interpret experimental results. Flamelet equations were solved in time and mixture fraction field, which was provided by non-reactive Large-Eddy Simulation (LES).

Keywords: MILD combustion, ethanol, dimethyl ether (DME), Jet in Hot Coflow (JHC)

1. Introduction

The ever-rising concern for the environment has increased efforts to improve energy efficiency and reduce pollutant emissions. Amongst advanced combustion technologies, Moderate or Intense Low-oxygen Dilution (MILD) combustion is a promising technology because of its potential to reduce emissions while maintaining a high thermal efficiency [1]. In practical devices, MILD combustion is usually established through a strong recirculation of hot exhaust gases. This leads to volumetric reactions without visible flames under some conditions [1, 2]. Hence it is also referred to as flameless oxidation (FLOX®) [1]. Under MILD combustion conditions the peak flame temperature is reduced due to a larger total volume of gases and the altered chemistry at a lower local oxygen concentration. Consequently, this causes a drastic reduction in emissions,

---

*Corresponding author
Email address:* `jingjing.ye01@adelaide.edu.au` (Jingjing Ye)

particularly in nitrogen oxides [3, 4].

Previous studies of MILD combustion [5, 6, 7, 8, 9] have mostly focused on common fossil fuels. There are limited studies that investigate MILD combustion of renewable fuels [10, 11]. Experimental measurements performed on the Jet in Hot Coflow (JHC) burner revealed a similar reaction zone structure of natural gas, ethylene, and LPG flames when hydrogen was added to the three fuels. This suggests different types of fuels are interchangeable under MILD combustion conditions [12]. Supporting this, Derudi and Rota [4] have reported that the averaged flame temperature and pollutants emissions were similar for methane and LPG flames when they were burnt in the MILD combustion mode. Whilst it is true that some previous studies have shown that for simple fuels the flame characteristics under MILD combustion conditions are very similar [4, 12], this is not true for more complex fuels [8, 13, 14]. For instance, visible flames and high NO_x emissions were reported as distinctive features when heavy fuel oil was used instead of light fuel oil in a MILD furnace [8]. Reddy et al. [13] found that lower NO_x and unburned hydrocarbon emissions were produced when a combustor was fired with a mixture of biodiesel and diesel rather than pure biodiesel. Ye et al. [14] performed a comparative study of ethanol, acetone, and n-heptane in a reverse-flow MILD combustor. They found that combustion of acetone and n-heptane became unstable at equivalence ratios of 0.7-0.8 and elevated pressures, where visible flames and high emissions were observed [14]. Meanwhile, stable combustion of ethanol was established under all the investigated conditions [14].

A better understanding of the impact of fuel type on the flame structure is required, particularly for fuels that are more complex than methane and hydrogen. Due to increasing interest in reducing the dependence on petroleum-derived fuels and diversifying the energy supply, alternative fuels have received great attention. Combining alternative fuels with MILD combustion would exploit the benefits of both, leading to more efficient combustion with lower emissions. Ethanol (CH_3CH_2OH) and dimethyl ether (CH_3OCH_3), isomers of C_2H_6O, are very promising fuels. Comparing them also provides an opportunity to explore the impact of molecular structure on the flame behaviour under vitiated coflow conditions.

Ethanol (EtOH), a type of alcohol, has a low tendency to generate soot and particulate-matter [15]. Due to its high flame speed it can be burnt at very lean conditions with a relatively low flame temperature [16]. As a consequence, NO_x emissions are suppressed. Ethanol can be produced from a wide range of renewable raw materials. Second generation bio-ethanol is derived from lignocellulosic biomass like wood, which is not in competition with food chain [17]. Its renewable nature, low emissions, and reduced production costs make it an attractive alternative fuel [18].

Dimethyl ether (DME), the simplest ether, is an excellent alternative fuel for transportation and power generation [19]. For instance, DME can be used as a substitute for diesel fuels due to its capacity to abate soot emissions [20]. The existence of an O atom and absence of any C-C bonds in DME contribute to its smoke-free nature [21]. It is also an ideal ignition promoter in engines not only because of its low auto-ignition temperature and high cetane number, but also because of its rapid vaporisation upon injection [20]. It can be manufactured from a variety of resources such as natural gas, wastes, and biomass [20].

Due to the potential utility of DME in gas turbine applications, the comparison between DME and methane (main component of natural gas) has attracted great interest. Lee and Yoon [22] tested DME in a

gas turbine, and they reported that lower NO_x emissions were produced from DME than methane. Chen et al. [23] investigated the impact of adding DME to methane-air flames on the ignition characteristics. They found that the ignition delay times of the methane-air mixture were significantly shortened due to a rapid build-up of CH_3 and HO_2 radicals with the presence of DME [23].

Limited comparative studies [24, 25, 26, 27, 28, 29, 30, 31, 32] have been performed to investigate the effect of molecular structure on the combustion behaviour of DME and ethanol flames. Most of these studies were focused on the role of the structure of oxygenated fuels in reducing soot precursors and soot particulates.

Previous studies have investigated the autoignition and extinction characteristics of ethanol and DME [25, 33]. Wang et al. [25] reported that DME flames were more resilient to extinction than ethanol flames, though this difference decreased as the fuel jet became more diluted with N_2 [25]. Tingas et al. [33] performed an analytical analysis of the autoignition characteristics of ethanol/air and DME/air homogeneous mixtures at an initial pressure of 5 MPa and an initial temperature of 1100 K. This analysis revealed an overall shorter ignition delay in the ethanol/air case. They found that the C-C bond in ethanol is maintained and the hydrogen chemistry plays a dominant role at the early stage of autoignition [33]. In contrast, the autoignition of DME/air is initiated by single-carbon chemistry [33]. As the reaction progresses, similar hydrogen chemistry pathways dominate in both fuels [33]. Formaldehyde was reported to be insignificant in the autoignition dynamics of ethanol/air mixtures, while adding formaldehyde can promote or retard the ignition of DME/air mixtures depending on the initial temperature [34].

There is a paucity of information on ethanol and DME flames under conditions relevant to MILD combustion. Kang et al. [10] investigated NO_x emissions of DME flames in a MILD burner. They found that the NNH-intermediate pathway was the major route for NO_x formation in DME flames under MILD combustion conditions [10]. Rodrigues et al. [11, 35] studied the ethanol spray flame structure in a hot and vitiated coflow. An enhanced spray evaporation in the presence of hot coflow led to changes in the atomisation mechanism, with an immediate liquid jet break-up near the atomiser [11]. Moreover, the reduced local oxygen concentration shifted the stoichiometric mixture fraction away from the spray axis, consequently reducing the peak flame temperature [11]. The liftoff heights of the ethanol spray flames were found to be dependent on the droplet convective, vaporisation, and chemical time scales before ignition [35].

The present paper aims to improve the understanding of the impact of fuel structure on MILD flames by performing a combined experimental and computational investigation of ethanol and DME. In order to control parameters independently, a JHC burner was used to emulate a MILD furnace environment where the gas mixture inside the combustion chamber is hot and diluted, with a fuel stream injecting into it. In this configuration, DME or prevaporised ethanol was issued into a hot and diluted coflow with the O_2 level varying from 3%-9% (by volume). To reveal the flame structure of the two fuels, the distributions of OH, CH_2O, and temperature have been measured instantaneously and simultaneously. Digital photographs and images of OH* chemiluminescence have also been recorded. To help explain the experimental observations, laminar flame calculations using the OPPDIF code and unsteady flamelet simulation have been performed. The purposes of the simulations in this paper are not to directly simulate the experimental flames. Instead, numerical simulations and experimental observations complement each other. The steady-state OPPDIF

3

T_{cofl} (K)	X_{O_2}	X_{H_2O}	X_{CO_2}	X_{N_2}	Z_{st}
1250	0.091	0.107	0.036	0.766	0.0863
1250	0.061	0.107	0.036	0.797	0.0597
1250	0.030	0.107	0.036	0.827	0.0305

Table 1: List of coflow conditions: T_{cofl} is the coflow temperature measured by a thermocouple after correction for radiation. The mole fractions of species in the coflow were determined by equilibrium calculations, and confirmed with measurements with a gas analyser.

analysis was performed to compare the chemistry of the two isomers, ethanol and DME, particularly via reaction flux analysis. This configuration is ideally suited to focusing on the fuel chemistry while isolating the impact of turbulence that occurs in the experiments. The unsteady flamelet model was employed to provide information on the transient ignition processes of the two fuels.

2. Experimental Details

2.1. Experimental Setup and Operating Conditions

The basic configuration and operation of this JHC burner shown in Fig. 1 are the same as in a previous study [36]. The JHC burner consists of an insulated central fuel jet (ID = 4.6 mm) surrounded by an annular coflow (ID = 82 mm). This coflow is generated from a secondary porous-bed burner located 90 mm upstream of the jet exit plane. The hot vitiated coflow was produced from the combustion of a lean mixture of natural gas (92% methane by volume), hydrogen, air, and nitrogen. The mole fractions of natural gas, hydrogen, air and nitrogen were manipulated to vary the coflow oxygen level from 3% to 9% by volume, while the temperature and C/H ratio were kept constant. The temperature of various coflows (T_{coflow}) was kept at 1250 K. The three hot coflow conditions are summarised in Table 1. To obtain a fully developed turbulent pipe flow, the length of the central fuel jet is more than 100 times the jet diameter. The burner was wrapped with ceramic fibre insulation to minimise heat losses and maintain a constant temperature of the coflow.

As shown in Fig. 1, ethanol was heated and mixed with carrier gas in a Controlled Evaporator and Mixer (CEM). The temperature of the heater inside the CEM was set by the Bronkhorst control unit, which also controlled the mass flow rates of ethanol and carrier gas. The preheat temperature was around 413 K, which is higher than the boiling point of ethanol (T_{boil} = 352 K). Furthermore, the pipeline was wrapped with insulation to minimise heat losses and prevent condensation. After prevaporisation, ethanol was carried by N_2 into the JHC burner via the central fuel jet. Dimethyl ether was mixed with N_2 and injected to the JHC burner directly. The jet Reynolds number for both ethanol and DME flames was kept around 10,000. It should be noted that the mole fraction of N_2 in the fuel jet was maintained at 0.59 for both fuels. In this case, due to the same chemical formula, the stoichiometric mixture fractions (Z_{st}) for both fuels are the same in a given coflow. The value of Z_{st} is 0.0305, 0.0597, and 0.0863 in the 3%, 6%, and 9% O_2 coflow, respectively.

A slot burner was mounted in the same field of view as the JHC burner to provide reference and calibration for image processing. The rectangular slot burner consists of a central fuel slot with an air slot on each side. Partially-premixed natural gas and air were fed through the central slot at a low velocity, coflowing by two streams of low-velocity air. This setup produced a straight and laminar flame. Hence, variations in the signal of this laminar flame can be considered solely due to the laser energy fluctuations.

[Figure 1 about here.]

2.2. Optical Setup

Imaging of flames was achieved through conventional photography, OH* chemiluminescence, Rayleigh scattering, and laser-induced fluorescence of OH (OH-LIF) and CH_2O (CH_2O-LIF). The photographs of the flames were taken using a Canon EOS 60D SLR camera with a standard 50 mm f/1.8 lens. The chemiluminescence of OH* was detected with an electronically-gated pco.pixelfly camera, equipped with a Lambert Instruments intensifier. The camera system was coupled with a 50 mm f/3.5 UV transmissive lens and a 310 nm bandpass optical filter with a bandwidth of 10 nm.

Rayleigh scattering was used to determine the temperature distribution of the flames. A frequency-doubled Nd:YAG laser was used to generate a 532 nm laser beam. The measured output energy was approximately 90 mJ/pulse before the slot burner. The detection of Rayleigh scattering signal was via a Princeton Instruments intensified CCD (ICCD) camera equipped with a 50 mm f/1.4 lens, which was mounted normal to the laser sheets. No visible particulate-matter and soot were observed during the experiments. Thus in order to maximise the collected Rayleigh signal, no filter was mounted in front of the collecting lens.

The A-X (1,0) $Q_1(7)$ line (283.222 nm) was chosen to excite OH due to its low sensitivity to ground-state population distribution in the expected temperature range [37]. A Q-smart 850 pulsed Nd:YAG laser was used to pump a Lambda-Physik ScanMate 2E dye laser at 532 nm with Rhodamine 6G dye. The output of the dye laser was frequency doubled to match the A-X (1,0) $Q_1(7)$ line. The energy of the OH laser was measured to be 0.9 mJ/pulse before the slot burner. The OH-LIF signal was detected with a Princeton Instruments ICCD camera, fitted with a 78 mm f/3.8 standard UV lens. This camera was mounted parallel to the laser sheets. A dichroic mirror was mounted in front of the lens of the OH camera at a 45 degree angle to the laser sheets. This mirror has a greater than 80% reflectance in the range of 270 to 340 nm, thus acting as a bandpass filter.

A frequency-tripled Nd:YAG laser was used to generate a 355 nm beam to excite CH_2O. The measured output energy was approximately 32 mJ/pulse before the slot burner. The CH_2O-LIF signal was collected with an Andor iStar ICCD camera, equipped with a 50 mm f/1.4 lens. Detection of formaldehyde was through a combination of long-wave-pass Andover Optics 395 FG03-50 and short-wave-pass Andover Optics 450 FL07-50 filters. The 532 nm, the 283.222 nm and the 355 nm laser sheets overlapped with each other and formed co-planar laser sheets. The heights of the 532 nm and 355 nm laser sheets were approximately 20 mm, while the 283.222 nm laser sheet was slightly shorter. Imaging from the central 8 mm of the laser sheets is presented in this paper.

5

2.3. Image Processing

Each instantaneous image from the three ICCD cameras was corrected for dark charge, detector atten-
uation, background, and laser energy variations. To correlate the information on the three images to each
other, the three images were matched such that each corresponding pixel in them represents the same physical
location. The resolution of these techniques was estimated to be 250 microns through imaging of a target at
the same plane as the laser sheets. The actual spatial resolution may vary due to several factors, such as the
laser sheet thickness (approximately 200 microns).

The quantification procedure of Rayleigh scattering is briefly described here. Further detail can be found
in Supplementary Material and a previous study by the authors [38]. To provide reference for temperature
quantification, a slot burner with a known laminar flame was installed upstream the JHC burner in the laser
path. Rayleigh scattering signal from this reference flame and the flame of interest was recorded in the same
image simultaneously during the experiments. A new variable T^* was introduced and defined as the ratio
of temperature (T) and effective Rayleigh cross-section (σ_{eff}). It is inversely proportional to the scattered
signal (I_R) as shown in equation (1). Thus, given the information of the reference flame, an image of T^* can
be generated from Rayleigh scattering image directly.

$$T^* = \frac{T}{\sigma_{eff}} = \frac{1}{I_R}\frac{T_{ref}I_{ref}}{\sigma_{eff,ref}} \tag{1}$$

Laminar flame calculations were employed to estimate temperature and effective Rayleigh cross-sections
as a function of mixture fraction, from which the relationship between σ_{eff} and T^* was drawn. Based on this
relationship, an image of the effective Rayleigh cross-section was interpolated from the image of T^*. This
relationship is independent of strain rate. However, it varies with the progress of the reaction. The effective
Rayleigh cross-section changes monotonically with T^* for a non-reacting mixture. For a reacting mixture,
the σ_{eff} decreases gradually with the increasing T^* until it reaches its peak value in the fuel-rich region. In
the fuel-lean region and the reaction zone, the σ_{eff} slightly increases with the increasing T^*. This is because
the Rayleigh cross-section of ethanol or DME is seven times higher than that of the hot oxidiser, while the
Rayleigh cross-sections of the hot oxidiser and combustion products are similar. The location of the peak T^*
was found to match the location of the peak number density of OH. During the interpolation of σ_{eff}, the
peak OH-LIF signal at each row was compared to a threshold value. If it was lower than the threshold value,
the mixture was considered to be non-reacting, thus σ_{eff} was interpolated from T^* based on the monotonic
relationship. If it was higher than the threshold value, the location of the peak OH-LIF signal was then
used to identify the boundary between the fuel-rich and the fuel-lean regions. Hence, the effective Rayleigh
cross-section can be interpolated correspondingly. The product of σ_{eff} and T^* gave the final temperature.

Quantification of Rayleigh scattering is limited to the bottom part of a flame in this study. Some OH
layers were distorted due to the flow vortex structure, particularly at the downstream of the flame. In this
case, there is no straightforward boundary between the fuel-lean and the fuel-rich region, and Rayleigh cross-
sections cannot be determined. Thereby, Rayleigh scattering images downstream were not used in this paper.
It is worth noting that the Rayleigh cross-section of each species was assumed to be constant at different
temperature. The error associated with this assumption was reported to be less than 2% for a temperature

6

range from 300 K to approximately 2200 K and when a 532 nm laser beam was used as the light source [39]. To evaluate the accuracy of the Rayleigh thermometry, the averaged coflow temperature measured with Rayleigh scattering is compared to that measured with a thermocouple. The differences between the two techniques typically do not exceed 5%. This indicates the suitability and accuracy of Rayleigh scattering quantification using the estimated effective Rayleigh cross-sections.

The OH-LIF results were semi-quantified with an estimated 20% error [40]. Specifically, the collisional cross-section and quenching rate coefficient as a function of temperature were obtained from a previous study by Tamura et al. [41]. The temperature distribution in mixture fraction space was estimated through laminar flame calculations. The calculated quenching rate for each flame was found to be constant across the reaction zone at various strain rates, hence a single value was used for each case. Boltzmann population distribution of OH at X-state with $v'' = 0$ and $J'' = 7.5$ was found to be relatively constant with the flame temperature ranging from 1000 K to 2000 K [40]. The peak OH number density of the steady laminar flame in the slot burner was calculated to be 2.1×10^{16} molecules/cm^3, which was used to calibrate the OH number density in the ethanol and DME flames.

It should be noted that the CH_2O signal was not quantified in the present study. However, because of the same geometry and facility, and the small temperature change in the fuel-rich region, the CH_2O signal is expected to reflect the relative quantity of CH_2O in various cases. Furthermore, previous studies [42, 43] reported that the temperature dependence of the CH_2O partition function and its quenching rate partially compensate for each other within a temperature range of 500 K to 1600 K. Therefore, the CH_2O-LIF signal is considered to be proportional to the number density of CH_2O within 15%–25% [42, 43].

3. Experimental Results and Discussion

3.1. Visual Observations

Figure 2 presents photographs of DME (left) and ethanol (right) flames carried by nitrogen under the three coflow conditions (3%, 6%, and 9% O_2 by volume). These photographs were taken with the same camera settings and presented with the same colour scale. None of the investigated flames emitted smoke or particulates during the experiments. All the photographs were split into red, green, and blue channels, and only the blue channel is displayed, indicating the CH* chemiluminescence near 430 nm [44]. The bottom edge of all the photographs coincides with the jet exit plane. Parts of the photographs appear saturated as this universal colour scale is chosen to emphasise the low signal from the flames in the 3% O_2 coflow. A previous study on the same JHC burner [37] reported that the entrainment of the surrounding air starts to affect the jet flame at approximately 100 mm above the jet exit plane (X/D = 22, where X is the axial distance above the jet exit plane and D is the jet diameter). The present study is only focused on the coflow-controlled region.

In a given coflow, DME flames always appear more lifted than ethanol flames. For both fuels, the flame shape and appearance are similar between the 6% and 9% O_2 coflows, despite minor differences in the flame luminosity. When the coflow O_2 level reduces to 3%, the flame luminosity is drastically lower, especially near

7

the flame base, therefore the exact liftoff height cannot be identified without ambiguity. Natural gas and ethylene flames issuing into a hot coflow with lower oxygen concentration were also reported to have faint flame bases [45, 46].

Under conventional combustion, an increase in the oxygen level in the oxidant stream is expected to cause a decrease in the liftoff height as the reactivity of the mixture is enhanced. However, as shown in Fig 2, the apparent liftoff heights of the ethanol flames are comparable under three coflow conditions. The liftoff height of the DME flame in the 3% O_2 coflow is also similar to that in the 6% O_2 case. The flame in the 9% O_2 case was slightly less lifted. This unusual trend in the liftoff height indicates that the flame stabilisation mechanism under conditions relevant to MILD combustion may be different from that in conventional combustion.

[Figure 2 about here.]

3.2. OH* chemiluminescence

A mean image of OH* chemiluminescence is averaged from 140 images taken with a gate time of 1 ms. The maximum OH* signal at a given height in the mean image after correcting for background is referred to as the peak intensity of OH* chemiluminescence. This is presented as a function of X/D for the ethanol and the DME flames in Fig. 3.

[Figure 3 about here.]

The peak intensity of OH* chemiluminescence increases substantially with the coflow O_2 level for both fuels. This is consistent with the increased flame luminosity shown in Fig. 2. A previous study on MILD combustion of methane using a jet-in-cross-flow burner reported that minor changes were found in the intensity of OH* chemiluminescence as the oxygen level increased [47]. The coflow temperature and oxygen level were strongly coupled in the previous study, however they are independent of each other in the current work. This may account for the discrepancy in the trend of OH* chemiluminescence.

Figure 3(b) displays the OH* profiles in the region between X/D = 3 - 10. It shows that given the same fuel, the growth in the OH* chemiluminescence is initiated nearly at the same axial location under the three coflow conditions. For instance, the signal of OH* chemiluminescence started to increase approximately at X/D = 5 for ethanol in various coflow cases.

The coflow O_2 level also affects the evolution of the build-up of the OH* chemiluminescence. For the ethanol flames in the 6% and 9% O_2 coflow, the peak intensity of OH* chemiluminescence increases rapidly over a small distance until it reaches its maximum, which is then followed by a decline in the intensity. In contrast, the peak intensity of OH* chemiluminescence from the ethanol flame in the 3% O_2 coflow increases gradually along the axial direction with a much smaller spatial gradient. The peak OH* chemiluminescence has been found to correlate to the peak temperature and the peak heat release rate in methane [48] and ethanol flames [49]. Therefore, in comparison with flames in the 6% and 9% O_2 coflows, a more spatially distributed temperature and heat release can be deduced from the OH* profile in the 3% O_2 case. Based on the distributed nature of MILD combustion [1, 50, 51], flames in the 3% O_2 coflow agree better with MILD combustion conceptually than flames in the coflow with a higher oxygen level.

8

The coflow O_2 level shows the same impact on the build-up of OH* chemiluminescence for the DME flames. However, in comparison with the ethanol flames, the rapid increase in the peak intensity of OH* chemiluminescence initiates further downstream in the DME flames. For instance, in the 6% O_2 coflow the OH* chemiluminescence signal starts to increase around X/D = 10, where the flame base is located in the photograph shown in Fig. 2. Under the same coflow conditions, the peak intensity of OH* chemiluminescence in the DME flames is considerably lower than that in the ethanol flames.

3.3. Instantaneous images: impact of coflow O_2 level

A selection of instantaneous OH (top), CH_2O (middle), and temperature (bottom) image triplets for the ethanol flames in the 3% and the 9% O_2 coflow are displayed in Fig. 4. Mean image triplets are included in the Supplementary Material. The centre of the images is at X/D = 3.15 (14.5 mm), X/D = 4.89 (22.5 mm), and X/D = 6.41 (29.5 mm) above the jet exit plane. The color scale is chosen to emphasise the low OH and CH_2O signals, hence some images with strong signals appear saturated. The instantaneous OH, CH_2O and temperature images were smoothed with a median filter to enhance the apparent signal-to-noise ratio.

At X/D = 3.15 above the jet exit plane, a faint OH signal, approaching the detection limit of the current setup, is observed from ethanol flames in the 3% O_2 coflow. This indicates a small quantity of OH was formed at this height. At X/D = 4.89 and X/D = 6.41, a higher level of OH was produced at approximately R/D = 2 in the ethanol flame in the 3% O_2 coflow. The OH layer was uniformly distributed across the entire laser sheet vertically.

The OH structure of the ethanol flame in the 9% O_2 coflow displays subtle, but important, differences in comparison with that in the 3% O_2 coflow. A similar level of faint OH signal is also observed at X/D = 3.15, however the OH level becomes significantly higher at X/D = 4.89 and X/D = 6.41 in the 9% O_2 case, suggesting a higher spatial gradient of OH than the 3% O_2 case. This agrees with a sharp increase in the OH* chemiluminescence in the 9% O_2 case, as shown in Fig. 3. Figures 4(e) and (f) also show that a thin region of weak OH "tail" exists upstream of a wide and defined region of strong OH. The occurrence of this kind of structure, referred to as a transitional flame structure, has been reported for ethylene-based flames in a coflow with 9% but not with 3% O_2 by volume [12]. This feature has previously been utilised to identify the transition away from the MILD combustion regime as the coflow oxygen level increases [52].

Along with a small quantity of OH, a considerable amount of CH_2O is measured in the fuel-rich region in the 3% and 9% O_2 cases. This further supports that reactions have already started at X/D = 3.15. This is in accordance with the common observation that CH_2O is the ignition precursor in flames issuing into a hot vitiated coflow [53, 54]. The CH_2O signal increases substantially with the axial distance, meanwhile its spatial distribution is broadened downstream.

The CH_2O signal of flames within the 9% O_2 coflow is lower than that in the 3% O_2 coflow, particularly near the jet exit plane. A previous study on methane flames [6] found that the oxygen level at the location of peak CH_2O was higher in the 3% case than the 9% case, resulting from an enhanced transport of O_2 to the fuel-rich side in the 3% case. Taking into account of the quenching effect of oxygen, the number density of CH_2O inferred from the LIF signal is underestimated in the 3% case. Therefore, a higher CH_2O-LIF

signal in the 3% case indeed indicates a higher number density of CH_2O than the 9% case. Typical of stable intermediates, the evolution of CH_2O is subject to convective-diffusive transport effects, as well as chemical kinetics effects [55]. The higher oxygen level at the location of peak CH_2O was found to cause an increase in CH_2O production for methane flames [6]. This could be responsible for a higher CH_2O number density in the 3% O_2 case, although it is acknowledged that the chemical kinetics impacts of O_2 levels on CH_2O formation might be dissimilar between ethanol and methane flames.

The temperature distribution of flames in the 3% and the 9% O_2 coflow is similar. The temperature images show a cold fuel-rich region and a hot coflow region with a uniform distribution of temperature. The temperature in the fuel-rich region increased gradually with the axial distance as more fuel was mixed with the hot coflow along the axial direction. For instance, this temperature change is evident by the colour changing from black in Fig. 4(d) to deep red in Fig. 4(f) near the jet centreline. Meanwhile, a moderate temperature region (800-1000 K) was shown to expand from R/D≈1 to 2. At X/D = 4.89 and X/D = 6.41, a well-defined region of OH is observed, and there is no noticeable temperature increase at the corresponding locations. The lack of correlation between the OH formation and the temperature increase was also reported in ethylene flames in a previous study on the same JHC burner [36].

[Figure 4 about here.]

3.4. Instantaneous images: impact of fuel type

Ethanol (CH_3-CH_2-OH) and DME (CH_3-O-CH_3) have the same number of C, H, and O atoms, but different chemical structure. Their distinct chemical structure is expected to cause differences in the flame structure.

Figures 5 and 6 display a selection of instantaneous OH (top), CH_2O (middle), and temperature (bottom) image triplets for the ethanol and the DME flames in the 3% and the 9% O_2 coflows, respectively. A higher CH_2O-LIF signal is observed in the DME flames than in the ethanol flames at a given axial distance. On average, the CH_2O signal in the DME flames is twice that in ethanol flames under the same coflow conditions. A previous study by Gabet et al. [56] also reported a strong CH_2O-LIF signal in DME flames in comparison with the methane-based flames.

The OH signal is slightly higher in the DME flames than in the ethanol flames at X/D = 3.15. Further downstream, the coflow oxygen level produced the same effects on the OH structure in the DME flames as in the ethanol flames. Specifically, a spatially distributed OH layer is observed approximately at R/D = 2 in the DME flame issuing into the 3% O_2 coflow. As for the 9% O_2 case, the OH level increases rapidly with the axial distance, and a transitional flame structure is shown at X/D = 6.41.

In summary, the coflow oxygen level shows the same impact on the distribution and build-up of OH and CH_2O for the ethanol and the DME flames. However, the intensity of OH-LIF and CH_2O-LIF signals vary between these two fuels, indicating different levels of OH and CH_2O were produced. Particularly, the OH and CH_2O signals in the DME flames are higher than those in the ethanol flames upstream of the apparent lift-off height, despite that the DME flames appeared more lifted than the ethanol flames. These phenomena are further investigated via numerical studies later in this paper.

10

[Figure 5 about here.]

[Figure 6 about here.]

4. Reaction Flux Analyses of The Isomers

A limited number of previous studies have focused on a direct comparison of DME and ethanol flames [24, 25, 26, 27, 28, 29, 30, 31, 57], most of which were for laminar and/or premixed flames. A few studies [25, 27] were performed on a counter-flow burner configuration in order to investigate the extinction and autoignition characteristics for the two fuels. Autoignition of ethanol flames was found to be delayed by the addition of DME, and the magnitude of this effect is dependent on strain rate [27]. It was also reported that DME flames were less prone to extinction than ethanol flames due to differences in the kinetics of intermediate species, such as formyl and methyl radicals [25]. However, experimental results in the present study show that these two fuels behave similarly under MILD combustion conditions in general. It is hypothesised that the H_2/O_2 pathways become dominant in the oxidation of both DME and ethanol due to a higher reactant temperature under MILD combustion conditions, resulting in their similarities.

In order to investigate this hypothesis and help interpret the experimental results, reaction path and sensitivity analyses should be performed. The oxidation of the fuels is initiated via fuel decomposition, including unimolecular decomposition and H atom abstraction reactions. It is necessary to analyse the fuel decomposition reactions in order to reveal differences in the initiation of the oxidation processes amongst the three fuels. Hence, primary kinetic pathways and sensitivity analysis should be performed at the mixture fraction where the peak fuel consumption rate occurs. To complement these results, analysis on the sensitivity of temperature to reaction rates across the whole mixture fraction domain is also required to demonstrate important features in the overall pyrolysis and oxidation processes. The Chemkin software is chosen for these reaction flux analyses as it provides built-in reaction path and sensitive analysis tools. In order to focus on the fuel chemistry and avoid the complexity of turbulence-chemistry interaction, laminar flame calculations of non-premixed flames at atmospheric pressure are performed with the OPPDIF code in the Chemkin software. These calculations are performed for steady flames, thus they are only relevant downstream of the stabilisation point.

All the calculations and analyses were carried out using a mechanism developed by Zhao et al. [58], consisting of 55 species and 290 reversible reactions. This mechanism consists of DME-related reactions and a baseline H_2/C_1-C_2 submodel developed for fuels like C_2H_5OH [58], which has been tested in previous studies [56, 57, 59, 60]. A multicomponent transport formulation is adopted while considering the effects of thermal diffusion in all the calculations.

A schematic of the opposed-flow flame setup is shown in Fig. 7. The fuel inlet is modelled as a cold mixture of N_2 (same concentration as the carrier N_2 in the experiments) and fuel: CH_3OCH_3, C_2H_5OH or ethane. Ethane (C_2H_6) is considered here for comparison to identify if a particular feature in a flame is caused by the existence of the O atom or by the different fuel structure. To reveal the impact of the presence of a hot and diluted coflow, the oxidiser inlet is modelled as cold air, a hot experimental coflow with 3%

11

or 9% O_2 by volume, which is referred to as air case, 3% O_2 case, and 9% O_2 case, respectively. The two opposing inlets are separated by 20 mm, and the momentum of the two inlets are balanced such that the stagnation plane is at X = 10 mm. Only results at a strain rate of 150 s^{-1} are presented in this subsection for brevity; however it is worth noting that the general trends are independent of strain rate.

[Figure 7 about here.]

The counter-flow configuration is not designed for simulating conventional lifted flames. Nonetheless, flames in a hot and vitiated coflow have been proven to behave in a totally different manner to those conventional lifted flames. The use of the OPPDIF code and the flamelet model in Section 5 is based on an assumption that autoignition is the dominant stabilisation mechanism for lifted flames in a hot and vitiated coflow. This assumption is supported by numerous experimental and numerical studies [36, 37, 46, 54, 61, 62, 63, 64, 65, 66, 67]. For instance, Cabra et al. [61] used probability density function (PDF) with the modified-Curl mixing model in a parabolic marching scheme to simulate lifted flames in a hot and vitiated coflow. This scheme only allowed autoignition for initial flame stabilisation, and good agreement was achieved between the simulation results and their experimental data [61]. These lifted flames measured by Cabra et al. [61] were also investigated by Ihme and See [62] using an unsteady flamelet/progress variable (UFPV) model. The UFPV model successfully predicted the autoignition process, and captured the temperature distribution and species concentration of these flames [62]. Luo et al. [63] performed a 3-D direct numerical simulation (DNS) of turbulent lifted flames in a hot coflow. They concluded that autoignition is the dominant flame stabilisation mechanism [63]. This conclusion has been validated by a number of studies on jet-in-hot-coflow configurations [36, 37, 54, 66, 67]. For instance, imaging of lifted flames in a Cabra burner [54] and a Dutch JHC burner [66, 67] revealed that the formation of autoignition kernels upstream of the liftoff height was responsible for stabilising the flame. An experimental study on the JHC burner [36, 37] also found that formaldehyde (CH_2O) was produced in significant quantities upstream the strong OH layer, indicating the occurrence of preignition reactions. The same phenomenon is also shown by CH_2O-LIF and OH-LIF results in the current study.

Numerical studies [48, 68] have attempted to use premixed flame models to investigate flames in a hot and vitiated oxidiser. Results from these studies indicate that models developed for conventional premixed flames are not suitable for studying lifted flames in a hot and vitiated oxidiser. For instance, Sidey et al. [48] reported high concentrations of CH_2O and H_2O_2 before the flame front for premixed flames diluted with hot products. They concluded that "as dilution increases significantly, the premixed flame approaches an autoignition problem", and specifically, that a "flame speed cannot be calculated above a certain dilution level" [48]. In order to demonstrate this, the PRMIX code was used to determine the flame speed of freely propagating and stoichiometric mixtures assuming adiabatic and atmospheric-pressure conditions. Two cases were investigated, including stoichiometric mixture of ethanol and air, and stoichiometric mixture of ethanol and hot oxidant with 9% oxygen. The calculated flame speed is presented in Table 2. Laminar flame speed for stoichiometric mixtures at room temperature was measured to be approximately 43 cm/s [69] and 45 cm/s [70] for ethanol and DME, respectively. The calculated laminar flame speed for ethanol is 41.7 cm/s,

12

Mixtures	Domain length			
	3 cm	5 cm	7 cm	10 cm
ethanol with air	41.7	41.7	41.7	41.7
ethanol with a hot oxidiser with 9% O_2	261.7	364.0	491.2	195.6

Table 2: Premixed flame speed (cm/s) for the air and hot oxidant cases at various domain lengths.

consistent with previous experimental measurement. However, the laminar flame speed for the hot oxidant case varied significantly with the domain size, suggesting that the results were not exclusively determined by intrinsic properties of the initial mixture. Similar results have also been reported by Habisreuther et al. [68]. They found that laminar burning velocity which matches with the unburned mixture velocity decreases as pressure increases when the inlet temperature is lower than the autoignition temperature [68]. However, at inlet temperatures higher than the autoignition temperature, the unburned mixture velocity increases rapidly with pressure due to a transition in flame structure triggered by ignition delay times [68].

4.1. Fuel chemistry comparison for the 3% O_2 case

Figure 8 illustrates primary kinetic pathways at the mixture fraction where the peak fuel consumption rate occurs in the 3% O_2 case. This demonstrates the major routes of fuel decomposition at that mixture fraction. The pathways start with the fuel, followed by the nine most important species containing carbon.

[Figure 8 about here.]

The existence of O atom is preserved during the decomposition of DME. Figure 8(a) demonstrates that the destruction of DME produces CH_2O, CH_3OCH_2, CH_3, CH_4, and CH_3O. One of the major intermediate species in the DME consumption path is CH_2O. The production of CH_2O is predominantly via β-scission after H-abstraction reactions: $CH_3OCH_3 \rightarrow CH_3OCH_2 \rightarrow CH_3+CH_2O$. Most of CH_2O is converted to formyl radical (HCO), subsequently converted to CO. The importance of CH_2O can also be inferred from its concentration. As displayed in Fig. 9(a), the concentration of CH_2O in the DME flames is significantly higher than the ethanol and the ethane flames. This is in accordance with imaging of CH_2O-LIF in the current experiments, where a higher CH_2O-LIF signal was collected from the DME flames than the ethanol flames at the same axial location.

[Figure 9 about here.]

The O atom is also retained during the consumption of ethanol. Figure 8(b) demonstrates that five main species, including C_2H_4OH, CH_3CHOH, CH_3CH_2O, C_2H_4, and CH_4, are formed following the destruction of ethanol. Some of these species are further converted to CH_3HCO mainly via hydrogen atom abstraction reactions. The vast production of CH_3HCO is an important feature in ethanol chemistry, which has been reported in previous studies [28, 30]. As shown in Fig. 9(b), the mole fraction of CH_3HCO in the ethanol flame is remarkably higher than that in the DME and the ethane flames.

13

In comparison with DME and ethanol, ethane is mainly converted to C_2H_5 via H-abstraction by H. Hence, the amount of unsaturated C_2 species in the ethane flame is expected to be considerably higher than that in the ethanol and the DME flames. Figure 10 displays a reduction in the concentrations of C_2H_4 and C_2H_2 in flames of oxygenated fuels, particularly DME. Higher yields of unsaturated C_2 species in the ethanol flame than the DME flame can be attributed to the formation of C_2H_4OH, which is subsequently decomposed to C_2H_4 and OH. In addition, due to the absence of a C-C bond, CH_3OCH_3 decomposes to CH_2O and CH_3 directly. This leads to a higher production of CH_4, as shown in Fig. 10(c).

The difference in the production of unsaturated C_2 species is not of great importance in the combustion of pure ethanol or DME. However, this should be taken into account when they are used as a fuel blend to reduce soot emissions. For instance, emissions of soot and particulates produced from heavy fuel oil were still high even when it was burnt in flameless combustion mode [8, 71]. The addition of oxygenated fuels to heavy fuel oil may help reduce these emissions.

[Figure 10 about here.]

More information regarding the fuel decomposition can be obtained from sensitivity analysis of the fuel concentration. This quantitatively shows how sensitive the fuel concentration is to the reaction rate of a particular reaction. As displayed in Fig. 11, for all three fuels the destruction of the fuel is most sensitive to the chain branching reaction $H+O_2 \rightleftharpoons O+OH$ (R1). The other common feature amongst the three fuels is that their concentration is sensitive to $CO+OH \rightleftharpoons CO_2+H$ (R29), which is one of the main contributors for heat release, thus promoting the consumption of the fuel. In comparison with ethanol and ethane, the concentration of DME is more sensitive to reactions involving methyl radical as shown in Fig. 11(a). Further analysis reveals that the production of methyl radical is significantly influenced by reaction R1 in the DME flame, contributing to the dominant importance of R1 in the fuel decomposition.

[Figure 11 about here.]

Results of temperature sensitivity are presented in Fig. 12. These results quantitatively demonstrate how sensitive temperature is to the reaction rate of a particular reaction. For all three fuels, reaction $H+O_2 \rightleftharpoons O+OH$ (R1) has the largest positive sensitivity coefficient, indicating the largest effect on increasing the temperature of the system. Reaction $CH_3+H(+M) \rightleftharpoons CH_4(+M)$ (R53) has the largest negative sensitivity coefficient and affects the temperature decrease the most. Consistent with the sensitivity analysis of the fuel consumption, temperature is also very sensitive to $CO+OH \rightleftharpoons CO_2+H$ (R29) for all three fuels.

To summarise, the differences in the fuel decomposition pathways in the 3% O_2 case affect the intermediate species pool considerably. This is reflected in the relative importance of intermediates, such as CH_2O, CH_3HCO, and CH_4. However, most of these differences in the chemical kinetics seem to play a minor role in the overall ignition and oxidation process as suggested by temperature sensitivity analysis. This analysis indicates the importance of H_2/O_2 pathways for all three fuels burning in a hot oxidiser with 3% O_2, which helps explain the similarities between the ethanol and the DME flames observed in the current experiments.

[Figure 12 about here.]

14

4.2. Fuel chemistry comparison for the air case

In order to better understand the impact of a hot and diluted oxidiser, calculations and sensitivity analyses were also performed for the three fuels burning in cold air (air case). Figure 13 shows that the peak flame temperature decreases by nearly 600 K as the oxidiser changes from the cold air to the 3% O_2 hot coflow. This matches with the usual observation of MILD flames with a reduced temperature increase. However, the temperature reduction is less than 200 K in the 9% O_2 case. The peak flame temperature of the three fuels is very close to each other when they are burning under the same oxidiser.

[Figure 13 about here.]

One interesting difference between the 3% O_2 case with the air case is found in the relative concentration of unsaturated C_2 species. To better depict the difference, the mole fractions of C_2H_4 and C_2H_2 are normalised to their peak mole fractions in the ethane flame at each case, as shown in Fig. 14. When oxygenated fuels are burnt instead of ethane, the reduction in the amount of unsaturated C_2 species is less significant in the air cases than the 3% O_2 cases. This indicates how intermediate species kinetics change with the oxidants. Fig. 14(b) and 14(e) also show the profiles of C_2H_4 and C_2H_2 in the 9% O_2 case, which resemble more closely the profiles in the air case rather than those in the 3% O_2 case. The fuel chemistry at the 9% O_2 case will be discussed in more detail in the following section.

[Figure 14 about here.]

Figure 15 presents the sensitivity analysis results of the destruction of each fuel at the mixture fraction, at which the peak fuel consumption rate occurs in the air cases. In contrast to the 3% O_2 cases, the concentration of each fuel does not show the largest sensitivity to $H+O_2 \rightleftharpoons O+OH$ (R1), but becomes more sensitive to fuel-specific reactions. For instance, the destruction of ethanol is most sensitive to $C_2H_5OH \rightleftharpoons C_2H_4+H_2O$ (R204).

[Figure 15 about here.]

The temperature sensitivity analysis also reflects differences between the 3% O_2 case and the air case. As shown in Fig. 16, reaction $H+O_2 \rightleftharpoons O+OH$ (R1) no longer has the largest positive impact on temperature. For all three fuels in the air case, temperature is mostly influenced by $H+OH+M \rightleftharpoons H_2O+M$ (R12), closely followed by $H+O_2(+M) \rightleftharpoons HO_2(+M)$ (R13). This shifted importance is suspected to result from a much lower initial temperature in the air case than the 3% O_2 case. Pellett et al. [72] reported that the reaction rates of R1 and R13 are balanced at the cross-over temperature approximately at 925 K at 1 atm. Hence, the lower temperature of air shifts the local temperature below the cross-over temperature, thereby promoting R13 over R1.

Important reactions become more different among the three fuels in the air case with respect to the 3% O_2 case, particularly in the fuel-rich region. In this region, reactions that have the largest positive/negative temperature sensitivities are mostly fuel-specific reactions with little shared similarities, such as $CH_3OCH_3 \rightleftharpoons CH_3+CH_3O$ (R239) in the DME flame, and $C_2H_4+H \rightleftharpoons C_2H_3+H_2$ (R119) in the ethanol flame.

15

The sensitivity analyses of the temperature and the fuel concentration suggest that the chemical pathways of three fuels become more different in the air case. Hence, ethanol and DME flames may be more dissimilar to each other when they are burnt in cold air instead of a hot oxidiser with 3% O_2.

[Figure 16 about here.]

4.3. Fuel chemistry comparison for the 9% O_2 case

Figure 17 shows a list of reactions that strongly affect the concentration of each fuel at the mixture fraction where the peak fuel consumption rate occurs in the 9% O_2 case. Interestingly, similar to the air case, these results indicate that fuel related reactions play a dominant role during the fuel decomposition process. Specifically, the concentrations of the three fuels are not very sensitive to $H+O_2 \rightleftharpoons O+OH$ (R1) and $CO+OH \rightleftharpoons CO_2+H$ (R29), different from results in the 3% O_2 case.

The reduced importance of reaction $H+O_2 \rightleftharpoons O+OH$ (R1) in the 9% O_2 case is also revealed by temperature sensitivity analysis, as shown in Fig. 18. Despite a very high initial temperature of the oxidiser, reactions of lower activation energy ($H+OH+M \rightleftharpoons H_2O+M$ (R12) and $H+O_2(+M) \rightleftharpoons HO_2(+M)$ (R13)) become more important than R1. Moreover, reactions that affect temperature the most in the 9% O_2 case are nearly the same as in the air case, regardless of large differences in the temperature and oxygen concentration of the oxidiser between these two cases.

In summary, sensitivity analysis results indicate that a three-fold increase in the oxygen concentration causes fundamental changes in the chemical kinetics of these fuels between the 3% and the 9% O_2 case. This can be used to explain why the ethanol and the DME flames shifted away from the MILD combustion regime as the oxygen concentration in the hot coflow increased from 3% to 9% in the current experiments.

[Figure 17 about here.]

[Figure 18 about here.]

5. Transient Ignition Processes of The Isomers

Reaction flux analyses in the preceding section were performed for steady opposed-flow laminar flames. However, the ignition of fuels is a time-varying process. Hence, an unsteady laminar flamelet analysis is presented to compare the transient ignition processes of the ethanol and the DME flames.

The unsteady flamelet model used here is similar to the model developed by Pitsch et al. [73]. This model has previously been applied, with a two-step analysis procedure, to simulate MILD flames in the same JHC configuration by Evans et al. [46]. To obtain the flow and mixture fields, non-reactive Large-Eddy Simulation (LES) was carried out. These simulations provided the temporal evolution of the flow field parameterised by the scalar dissipation rate of the mixture necessary for the second step. During the second step, unsteady flamelet equations were solved in time and mixture fraction space. The two simulation steps will be described in detail in the following sections.

The use of a flamelet model is supported by previous successful applications of a flamelet model to flames in a hot and diluted coflow [46, 62]. Flamelet-like structure has also been reported under MILD combustion

16

conditions [47, 74]. For instance, a three-dimensional DNS study of MILD methane flames by Minamoto and Swaminathan [74] identified thin reaction zone with flamelet-like behaviour. They found thin regions of intense reactions, demonstrating the existence of flamelets [74]. This finding is supported by an experimental study on MILD combustion by Sidey and Mastorakos [47] where a methane jet was injected into cross-flow of hot products. Instantaneous planar imaging of OH showed a sharp transition from regions without OH to regions with OH [47]. They concluded that MILD methane flame was burnt in thin and distinct regions despite a low flame luminosity [47].

5.1. Modelling approach - Large-Eddy Simulation

LES was carried out to obtain a solution of the turbulent flow field. The experimental configuration was simulated using a fully three-dimensional cylindrical grid with 256, 128, and 96 grid points in the axial, the radial, and the circumferential directions, respectively. The grid is stretched in the axial direction with a grid spacing of 0.5 mm at the jet exit plane. The radial grid sizing is 0.1 mm at the nozzle. The boundary conditions were set to match the experimental conditions. A well-resolved LES of the central fuel pipe upstream of the jet exit plane was run prior to the main simulations, which generates velocity data at the jet inlet boundary for the main simulations. For the inlet boundary condition of the coflow, a constant velocity profile is prescribed. A convective outlet condition is defined for the outlet of the domain. At the radial boundary of the simulation domain, zero gradient boundary conditions are imposed for either velocities or scalars, thus there is no flux at the boundaries in the radial direction.

The parallel, finite difference code CIAO was used for the LES. It solves the filtered Navier-Stokes equations in the low Mach number limit. The momentum equations are spatially discretized with a second-order scheme [75]. Spatial gradients of the scalar equation are discretized with a third order WENO scheme [76]. Unclosed subfilter terms are closed with a dynamic Smagorinsky model [77] with Lagrangian averaging [78] for the subfilter stress term and a Smagorinsky type model [79] for the subfilter diffusivity of the scalar equation. A scalar transport equation is solved for the filtered mixture fraction $\tilde{Z}$, which locally defines the state of the fluid mixture.

The scalar dissipation rate, determined from the flow-field solution, is defined as averaged conditional scalar dissipation rate at each grid plane in the axial direction. The distance to the jet exit plane can be related to the flamelet time via a characteristic velocity u_{st}, which is the mean axial velocity at the radial position where $\tilde{Z} = Z_{st}$ [73]. The relationship between the axial distance and the flamelet time is defined by [73]

$$t = \int_0^x \frac{1}{u_{st}|\,(Z = Z_{st})} dx'$$

(2)

Fluid properties, such as density, viscosity, and diffusivity of the scalar, are obtained from an extinct flamelet solution (χ above extinction strain rate), which is tabulated and accessed during runtime. During the second step, the unsteady flamelet model simulates the ignition process based on these fluid and turbulence properties. This analysis is only focused on the onset of ignition, and it assumes that changes in the conditional scalar dissipation rates are negligible due to a small temperature increase and limited heat release in the stabilisation region. Hence, these minor changes as a consequence of ignition are not incorporated into the

17

LES as feedback. Jochim et al. [80] found that for diesel engine combustion, this assumption can even lead to correct predictions of the major characteristics of the entire combustion process.

5.2. Modelling approach - Unsteady flamelets

For the solution of chemistry, the unsteady flamelet equations [81, 82] are solved in time and mixture fraction space using the FlameMaster program [83]. The unsteady flamelet equations are

$$\rho \frac{\partial T}{\partial t} - \rho \frac{\chi}{2} \left(\frac{\partial^2 T}{\partial Z^2} + \frac{1}{c_p} \frac{\partial c_p}{\partial Z} \frac{\partial T}{\partial Z} \right) + \frac{1}{c_p} \left(\sum_{k=1}^{N} h_k \dot{m}_k - \mathcal{H} \right) = 0 \tag{3}$$

where T denotes the temperature, t and Z are time and mixture fraction, respectively. χ denotes the scalar dissipation rate, ρ is the density, and c_p is the specific heat capacity at ambient pressure. N is the number of species included in the mechanism, h_k and $\mathcal{H}$ represent the enthalpy of species k and the enthalpy flux by mass diffusion, respectively.

The scalar dissipation rates and local compositions are extracted from the LES as described in the preceding section. They change with time and are coupled to the axial distance via the characteristic time. The mechanism used in the unsteady flamelets model is the same as in Section 4 [58].

5.3. Results and discussion

Figure 19 shows the peak temperature from the flamelet solution as a function of time for ethanol and DME flames in the 3% and 9% O_2 cases. The mixture fraction where the peak temperature occurs is denoted as Z_{Tpeak}. Temperature profiles at Z_{st} and the most reactive mixture fraction (Z_{mr}) are also included for comparison. The most reactive mixture fraction is a result of the competing effects of high temperature at a leaner mixture fraction and high fuel concentration at a richer mixture fraction [84].

The maximum peak temperature is very close for the two fuels. However, given the same oxidant stream, a rapid increase in the peak temperature takes place earlier in the ethanol flames, indicating a much faster ignition in comparison with the DME flames. In the current experiments, DME flames always appeared more lifted than ethanol flames, as revealed by digital photography and imaging of OH* chemiluminescence. The larger liftoff heights are likely to result from longer ignition delay times of DME flames at the conditions corresponding to the most reactive mixture fraction.

As the oxygen level reduces from 9% to 3%, the ignition process becomes prolonged with a reduced temperature increase for both ethanol and DME. This change is most prominent at Z_{st}, where the gradient of the temperature profile is considerably sharper in the 9% O_2 case than the 3% O_2 case. Thus, flames in the 3% O_2 case agree better with the definition of MILD flame being distributed with a low temperature increase [1, 50, 51].

The flame propagation process is reflected by the change in Z_{Tpeak} with time. As demonstrated in Fig. 19, the peak temperature initially occurs at a very low mixture fraction with a low scalar dissipation rate for both fuels. As the ignition process proceeds, the temperature increase slowly propagates to a higher mixture fraction region where the corresponding scalar dissipation rate (χ) is higher.

18

The peak flame temperature occurs at a relatively leaner condition in the DME flames than the ethanol flames, particularly at the onset of temperature rise. The scalar dissipation rates at a given peak temperature for the DME flames are lower than those in the ethanol flames. For instance, at the location where the peak temperature reaches 1600 K, the scalar dissipation rate is 0.8 1/s for DME, but it is 1.5 1/s for ethanol in the 9% O_2 case. Mastorakos [84] reported that the ignition delay time is mainly determined by the scalar dissipation rate at the most reactive mixture fraction in the cold-fuel-hot-oxidant configuration. The ignition of the DME flames occurs later and at a leaner condition than in the ethanol flames. This also means that the initial temperature of the flammable mixture is higher in the DME flames than the ethanol flames. As shown in Fig. 19 (the bottom figure), the scalar dissipation rate at a given mixture fraction decreases with time, and the scalar dissipation rate is lower in the leaner conditions at a given time. These results indicate that the ignition of DME requires a lower scalar dissipation rate and a higher initial temperature than ethanol, reflecting a lower reactivity of DME at the conditions investigated here. A series of steady flamelets calculations is performed to produce a S-curve of scalar dissipation rate and the corresponding maximum temperature for the various cases investigated. These results show that, given the same oxidant stream, the scalar dissipation rate of ignition on the lower branch of S-curve for DME is lower than that for ethanol. This agrees with a previous study by Loukou et al. [27], who found that autoignition of ethanol was retarded by the addition of DME.

[Figure 19 about here.]

In order to better depict the temporal evolution process, Fig. 20 presents temperature as a function of mixture fraction at four time steps, including when the temperature increase (ΔT) reaches 10 K, when ΔT = 100 K, when the most rapid change in temperature ($(dT/dt)_{max}$)) occurs, and when the maximum peak temperature occurs. The temperature increase (ΔT) is defined as the difference between the peak temperature in the whole mixture fraction domain and the initial temperature of the oxidiser. In the case of the DME flame burning in the 3% O_2 case, the peak temperature occurs at Z = 0.00805, Z = 0.0201, Z = 0.0201, and Z = 0.0362 at the four time steps, respectively. In the case of the DME flame burning in the 9% O_2 case, the peak temperature occurs at Z = 0.0161, Z = 0.0201, Z = 0.0564, and Z = 0.0926 at the four time steps, respectively. This shift in the mixture fraction at the four time steps in the ethanol flames is the same as the DME flames. The stoichiometric mixture fractions for both fuels are 0.0305 and 0.0863 in the 3% and 9% O_2 cases, respectively. Figure 20 shows that for both fuels, though the maximum temperature eventually occurs at a slightly richer mixture fraction than Z_{st}, the first temperature increase occurs at a much leaner condition, corresponding to the most reactive mixture fraction. The value of Z_{mr} indicates the dominant role of the hot oxidant temperature over the fuel concentration in the mixture reactivity.

[Figure 20 about here.]

Figure 21 shows the mole fractions of OH, HO_2, CH_3, CH_3OCH_2, and C_2H_4OH, which are normalised to their maximum mole fractions at Z_{mr}. Profiles of CH_3OCH_2 and C_2H_4OH are presented as these species are amongst the first products when the parent fuel is consumed via H-atom abstraction reactions. Normalised temperature profiles at Z_{mr} are also included to indicate the stage of the ignition process.

19

The species profiles show that the ethanol and the DME flames undergo different processes prior to the main ignition event. Here the main ignition event refers to the most rapid change in temperature $((dT/dt)_{max})$. For instance, there is a steady build-up of HO_2 radicals during the early phase of ignition featured with a moderate temperature increase in the DME flames. In the meantime, the concentrations of both CH_3 and CH_3OCH_2 change very slowly, particularly in the 3% O_2 case. For instance, during t = 5 ms to t = 25 ms, the concentration of CH_3OCH_2 is almost constant, while CH_3 is formed slowly in the 3% O_2 case. The consumption of HO_2 initiates at t = 33 ms and t = 26 ms in the 3% and 9% O_2 case, respectively. This process promotes chain-branching reactions and triggers the main ignition event.

The onset of ignition is initiated more rapidly in the ethanol flames than in the DME flames. In addition, during the early phase of ignition, the concentrations of HO_2, CH_3, and CH_3OCH_2 in the ethanol flames change much faster than in the DME flames. The steady opposed-flow flame analysis in Section 4 highlights the distinct fuel decomposition processes of ethanol and DME, which are related to the differences in the temporal evolution of intermediate species produced before the main ignition event. During the main ignition event, there is a rapid consumption of HO_2 and CH_3, in addition to a fast build-up of OH, in both the ethanol and the DME flames. Results from this unsteady flamelet model also show that the growth in the OH concentration occurs earlier in the ethanol flames than in the DME flames in the whole mixture fraction domain. This cannot explain the lower OH-LIF signals observed in the ethanol flames than in the DME flames at the same axial location in the current experiments, and a further study is required to understand this.

[Figure 21 about here.]

6. Conclusions

This paper presents a combined experimental and computational investigation of ethanol and DME flames under conditions relevant to MILD combustion. The distributions of OH, CH_2O, and temperature were recorded instantaneously and simultaneously. Imaging of OH^* chemiluminescence and digital photography were also performed to reveal the flame structure and the apparent liftoff heights. Steady laminar flame calculations using the OPPDIF code and an unsteady laminar flamelet analyses were conducted to help shed more light on the effect of the operating parameters on the chemical pathways and ignition process. The key findings arising from this study are:

- Under the same coflow condition, the overall spatial distribution and evolution of OH, CH_2O, and temperature were quite similar for ethanol and DME. The intensity of OH-LIF and CH_2O-LIF signals vary between these two fuels. Particularly, stronger CH_2O-LIF signals were measured from DME flames than ethanol flames as CH_2O is one of the major intermediate species in the DME chemistry.

- A transitional flame structure revealed by OH-LIF was observed in the ethanol and the DME flames issuing into the 9% O_2 coflow but not in the 3% O_2 coflow. The occurrence of this transitional flame structure suggests that the ethanol and the DME flames deviated away from the MILD combustion regime as the coflow oxygen level increased from 3% to 9%.

20

- Ethanol and DME are decomposed via different pathways, leading to differences in the intermediate species pool. However, temperature sensitivity analysis indicates that the differences in the fuel decomposition pathways play a minor role in the overall oxidation processes in the 3% O_2 cases. Under these conditions, the H_2/O_2 pathways are very important for both fuels, contributing to the similarities between them.

- When air and a vitiated oxidant stream with 9% O_2 are used instead of a vitiated oxidiser with 3% O_2, the flame temperature becomes more sensitive to fuel-specific reactions for each fuel. These results suggest that the chemical kinetics may change fundamentally due to a three-fold increase in the oxygen concentration. This explains why experimental ethanol and DME flames shifted away from the MILD combustion regime as the hot coflow oxygen level increased from 3% to 9%.

7. Acknowledgements

8. References

[1] J. Wünning, J. Wünning, Flameless oxidation to reduce thermal NO-formation, Prog. Energ. Combust. 23 (1) (1997) 81–94.

[2] G. G. Szegö, B. B. Dally, G. J. Nathan, Operational characteristics of a parallel jet MILD combustion burner system, Combust. Flame 156 (2) (2009) 429–438.

[3] I. Özdemir, N. Peters, Characteristics of the reaction zone in a combustor operating at mild combustion, Exp. Fluids 30 (6) (2001) 683–695.

[4] M. Derudi, R. Rota, Experimental study of the mild combustion of liquid hydrocarbons, Proc. Combust. Inst. 33 (2) (2011) 3325–3332.

[5] R. Sadanandan, R. Lückerath, W. Meier, C. Wahl, Flame characteristics and emissions in flameless combustion under gas turbine relevant conditions, J. Propul. Power 27 (5) (2011) 970–980.

[6] P. R. Medwell, P. A. M. Kalt, B. B. Dally, Reaction zone weakening effects under hot and diluted oxidant stream conditions, Combust. Sci. Technol. 181 (7) (2009) 937–953.

[7] A. Cavigiolo, M. A. Galbiati, A. Effuggi, D. Gelosa, R. Rota, Mild combustion in a laboratory-scale apparatus, Combust. Sci. Technol. 175 (8) (2003) 1347–1367.

[8] R. Weber, J. P. Smart, W. vd Kamp, On the (MILD) combustion of gaseous, liquid, and solid fuels in high temperature preheated air, Proc. Combust. Inst. 30 (2) (2005) 2623–2629.

21

[9] P. Li, B. B. Dally, J. Mi, F. Wang, MILD oxy-combustion of gaseous fuels in a laboratory-scale furnace, Combust. Flame 160 (5) (2013) 933–946.

[10] Y. Kang, T. Lu, X. Lu, Q. Wang, X. Huang, S. Peng, D. Yang, X. Ji, Y. Song, Study on combustion characteristics of dimethyl ether under the moderate or intense low-oxygen dilution condition, Energy Convers. Manage. 108 (2016) 549–565.

[11] H. C. Rodrigues, M. J. Tummers, E. H. van Veen, D. Roekaerts, Spray flame structure in conventional and hot-diluted combustion regime, Combust. Flame 162 (3) (2015) 759–773.

[12] P. R. Medwell, B. B. Dally, Effect of fuel composition on jet flames in a heated and diluted oxidant stream, Combust. Flame 159 (10) (2012) 3138–3145.

[13] V. M. Reddy, P. Biswas, P. Garg, S. Kumar, Combustion characteristics of biodiesel fuel in high recirculation conditions, Fuel Process. Technol. 118 (2014) 310–317.

[14] J. Ye, P. R. Medwell, E. Varea, S. Kruse, B. B. Dally, H. G. Pitsch, An experimental study on MILD combustion of prevaporised liquid fuels, Appl. Energy 151 (2015) 93–101.

[15] C. Esarte, M. Peg, M. P. Ruiz, A. Millera, R. Bilbao, M. U. Alzueta, Pyrolysis of ethanol: gas and soot products formed, Ind. Eng. Chem. Res. 50 (8) (2011) 4412–4419.

[16] A. H. Lefebvre, D. R. Ballal, Gas Turbine Combustion: Alternative Fuels and Emissions, Hoboken: Taylor and Francis, 2010.

[17] M. Balat, H. Balat, Recent trends in global production and utilization of bio-ethanol fuel, Appl. Energy 86 (11) (2009) 2273–2282.

[18] W. Leitner, J. Klankermayer, S. Pischinger, H. Pitsch, K. Kohse-Höinghaus, Advanced biofuels and beyond: Chemistry solutions for propulsion and production, Angewandte Chemie 129 (20) (2017) 5500–5544.

[19] D. Cocco, V. Tola, G. Cau, Performance evaluation of chemically recuperated gas turbine (CRGT) power plants fuelled by di-methyl-ether (DME), Energy 31 (10) (2006) 1446–1458.

[20] C. Arcoumanis, C. Bae, R. Crookes, E. Kinoshita, The potential of di-methyl ether (DME) as an alternative fuel for compression-ignition engines: A review, Fuel 87 (7) (2008) 1014–1030.

[21] H. Curran, W. Pitz, C. Westbrook, P. Dagaut, J. Boettner, M. Cathonnet, A wide range modeling study of dimethyl ether oxidation, Int. J. Chem. Kinet. 30 (3) (1998) 229–241.

[22] M. C. Lee, Y. Yoon, Development of a gas turbine fuel nozzle for DME and a design method thereof, Fuel 102 (2012) 823–830.

[23] Z. Chen, X. Qin, Y. Ju, Z. Zhao, M. Chaos, F. L. Dryer, High temperature ignition and combustion enhancement by dimethyl ether addition to methane-air mixtures, Proc. Combust. Inst. 31 (1) (2007) 1215–1222.

[24] C. S. McEnally, L. D. Pfefferle, The effects of dimethyl ether and ethanol on benzene and soot formation in ethylene nonpremixed flames, Proc. Combust. Inst. 31 (1) (2007) 603–610.

[25] Y. L. Wang, P. S. Veloo, F. N. Egolfopoulos, T. T. Tsotsis, A comparative study on the extinction characteristics of non-premixed dimethyl ether and ethanol flames, Proc. Combust. Inst. 33 (1) (2011) 1003–1010.

[26] K. H. Song, P. Nag, T. A. Litzinger, D. C. Haworth, Effects of oxygenated additives on aromatic species in fuel-rich, premixed ethane combustion: a modeling study, Combust. Flame 135 (3) (2003) 341–349.

[27] A. Loukou, J. Reiter, R. Gehmlich, C. Hasse, D. Trimis, E. Pucher, K. Seshadri, Autoignition and extinction of mixtures of ethanol and dimethyl ether, in: Proceedings of the European Combustion Meeting, 2015.

[28] A. Frassoldati, T. Faravelli, E. Ranzi, K. Kohse-Höinghaus, P. R. Westmoreland, Kinetic modeling study of ethanol and dimethyl ether addition to premixed low-pressure propene-oxygen-argon flames, Combust. Flame 158 (7) (2011) 1264–1276.

[29] T. Kitamura, T. Ito, J. Senda, H. Fujimoto, Extraction of the suppression effects of oxygenated fuels on soot formation using a detailed chemical kinetic model, JSAE review 22 (2) (2001) 139–145.

[30] J. Wang, U. Struckmeier, B. Yang, T. A. Cool, P. Osswald, K. Kohse-Höinghaus, T. Kasper, N. Hansen, P. R. Westmoreland, Isomer-specific influences on the composition of reaction intermediates in dimethyl ether/propene and ethanol/propene flame, J. Phys. Chem. A 112 (39) (2008) 9255–9265.

[31] B. A. V. Bennett, C. S. McEnally, L. D. Pfefferle, M. D. Smooke, M. B. Colket, Computational and experimental study of the effects of adding dimethyl ether and ethanol to nonpremixed ethylene/air flames, Combust. Flame 156 (6) (2009) 1289–1302.

[32] P. Pepiot-Desjardins, H. Pitsch, R. Malhotra, S. Kirby, A. Boehman, Structural group analysis for soot reduction tendency of oxygenated fuels, Combust. Flame 154 (1) (2008) 191–205.

[33] E. A. Tingas, D. C. Kyritsis, D. A. Goussis, Autoignition dynamics of DME/air and EtOH/air homogeneous mixtures, Combust. Flame 162 (9) (2015) 3263–3276.

[34] E. A. Tingas, D. C. Kyritsis, D. A. Goussis, Ignition delay control of DME/air and EtOH/air homogeneous autoignition with the use of various additives, Fuel 169 (2016) 15–24.

[35] H. C. Rodrigues, M. Tummers, E. van Veen, D. Roekaerts, Effects of coflow temperature and composition on ethanol spray flames in hot-diluted coflow, Int. J. Heat. Fluid Fl. 51 (2015) 309–323.

[36] P. R. Medwell, P. A. M. Kalt, B. B. Dally, Imaging of diluted turbulent ethylene flames stabilized on a jet in hot coflow (JHC) burner, Combust. Flame 152 (1) (2008) 100–113.

[37] P. R. Medwell, P. A. M. Kalt, B. B. Dally, Simultaneous imaging of OH, formaldehyde, and temperature of turbulent nonpremixed jet flames in a heated and diluted coflow, Combust. Flame 148 (1) (2007) 48–61.

[38] J. Ye, P. Medwell, M. Evans, B. Dally, Quantitative rayleigh temperature imaging in turbulent flames of prevaporised n-heptane, in: In Proceedings of the 7th Australian Conference on Laser Diagnostics in Fluid Mechanics and Combustion, The University of Melbourne, Australia, 2015, december 2015.

[39] G. Sutton, A. Levick, G. Edwards, D. Greenhalgh, A combustion temperature and species standard for the calibration of laser diagnostic techniques, Combust. Flame 147 (1) (2006) 39–48.

[40] P. R. Medwell, Laser diagnostics in MILD combustion, Ph.D. thesis (2007).

[41] M. Tamura, P. A. Berg, J. E. Harrington, J. Luque, J. B. Jeffries, G. P. Smith, D. R. Crosley, Collisional quenching of CH (A), OH (A), and NO (A) in low pressure hydrocarbon flames, Combust. Flame 114 (3) (1998) 502–514.

[42] D. C. Kyritsis, V. S. Santoro, A. Gomez, The effect of temperature correction on the measured thickness of formaldehyde zones in diffusion flames for 355 nm excitation, Exp. Fluids. 37 (5) (2004) 769–772.

[43] C. Brackmann, J. Bood, M. AldÉn, G. Pengloan, O. Andersson, Quantitative measurements of species and temperature in a DME-air counterflow diffusion flame using laser diagnostic methods, Combust. Sci. Technol. 178 (6) (2006) 1165–1184.

[44] J. Kojima, Y. Ikeda, T. Nakajima, Basic aspects of OH (A), CH (A), and C_2 (d) chemiluminescence in the reaction zone of laminar methane-air premixed flames, Combust. Flame 140 (1) (2005) 34–45.

[45] P. R. Medwell, B. B. Dally, Experimental observation of lifted flames in a heated and diluted coflow, Energy Fuels 26 (9) (2012) 5519–5527.

[46] M. Evans, P. Medwell, H. Wu, A. Stagni, M. Ihme, Classification and lift-off height prediction of non-premixed MILD and autoignitive flames, Proc. Combust. Inst. 36 (3) (2017) 4297-4304.

[47] J. Sidey, E. Mastorakos, Visualization of MILD combustion from jets in cross-flow, Proc. Combust. Inst. 35 (3) (2015) 3537–3545.

[48] J. Sidey, E. Mastorakos, R. Gordon, Simulations of Autoignition and Laminar Premixed Flames in Methane/Air Mixtures Diluted with Hot Products, Combust. Sci. Technol. 186 (4-5) (2014) 453–465.

[49] J. Ye, P. R. Medwell, B. B. Dally, M. J. Evans, The transition of ethanol flames from conventional to MILD combustion, Combust. Flame 171 (2016) 173–184.

[50] S. Kumar, P. Paul, H. Mukunda, Prediction of flame liftoff height of diffusion/partially premixed jet flames and modeling of mild combustion burners, Combust. Sci. Technol. 179 (10) (2007) 2219–2253.

[51] C. Duwig, B. Li, Z. Li, M. Aldn, High resolution imaging of flameless and distributed turbulent combustion, Combust. Flame 159 (1) (2012) 306–316.

[52] M. Evans, P. Medwell, Z. Tian, Modeling lifted jet flames in a heated coflow using an optimized eddy dissipation concept model, Combust. Sci. Technol. 187 (7) (2015) 1093–1109.

[53] P. R. Medwell, D. L. Blunck, B. B. Dally, The role of precursors on the stabilisation of jet flames issuing into a hot environment, Combust. Flame 161 (2) (2013) 465–474.

[54] R. L. Gordon, A. R. Masri, E. Mastorakos, Simultaneous Rayleigh temperature, OH- and CH_2O-LIF imaging of methane jets in a vitiated coflow, Combust. Flame 155 (1) (2008) 181–195.

[55] C. Fotache, T. Kreutz, C. Law, Ignition of counterflowing methane versus heated air under reduced and elevated pressures, Combust. Flame 108 (4) (1997) 442–470.

[56] K. N. Gabet, H. Shen, R. A. Patton, F. Fuest, J. A. Sutton, A comparison of turbulent dimethyl ether and methane non-premixed flame structure, Proc. Combust. Inst. 34 (1) (2013) 1447–1454.

[57] H. Xu, C. Yao, T. Yuan, K. Zhang, H. Guo, Measurements and modeling study of intermediates in ethanol and dimethy ether low-pressure premixed flames using synchrotron photoionization, Combust. Flame 158 (9) (2011) 1673–1681.

[58] Z. Zhao, M. Chaos, A. Kazakov, F. L. Dryer, Thermal decomposition reaction and a comprehensive kinetic model of dimethyl ether, Int. J. Chem. Kinet. 40 (1) (2008) 1–18.

[59] F. Herrmann, B. Jochim, P. Oβwald, L. Cai, H. Pitsch, K. Kohse-Höinghaus, Experimental and numerical low-temperature oxidation study of ethanol and dimethyl ether, Combust. Flame 161 (2) (2014) 384–397.

[60] Z. Chen, C. Tang, J. Fu, X. Jiang, Q. Li, L. Wei, Z. Huang, Experimental and numerical investigation on diluted DME flames: Thermal and chemical kinetic effects on laminar flame speeds, Fuel 102 (2012) 567–573.

[61] R. Cabra, J. Y. Chen, R. W. Dibble, A. N. Karpetis, R. S. Barlow, Lifted methane-air jet flames in a vitiated coflow, Combust. Flame 143 (4) (2005) 491–506.

[62] M. Ihme, Y. C. See, Prediction of autoignition in a lifted methane/air flame using an unsteady flamelet/progress variable model, Combust. Flame 157 (10) (2010) 1850–1862.

[63] Z. Luo, C. S. Yoo, E. S. Richardson, J. H. Chen, C. K. Law, T. Lu, Chemical explosive mode analysis for a turbulent lifted ethylene jet flame in highly-heated coflow, Combust. Flame 159 (1) (2012) 265–274.

[64] P. R. Medwell, M. J. Evans, Q. N. Chan, V. R. Katta, Laminar flame calculations for analyzing trends in autoignitive jet flames in a hot and vitiated coflow, Energy Fuels 30 (10) (2016) 8680–8690.

[65] M. J. Evans, P. R. Medwell, Z. F. Tian, A. Frassoldati, A. Cuoci, A. Stagni, Ignition characteristics in spatially zero-, one- and two-dimensional laminar ethylene flames, AIAA Journal (2016) 3255–3264.

25

[66] E. Oldenhof, M. Tummers, E. Van Veen, D. Roekaerts, Ignition kernel formation and lift-off behaviour of jet-in-hot-coflow flames, Combust. Flame 157 (6) (2010) 1167–1178.

[67] E. Oldenhof, M. J. Tummers, E. H. Van Veen, D. J. E. M. Roekaerts, Transient response of the Delft jet-in-hot coflow flames, Combust Flame 159 (2) (2012) 697–706.

[68] P. Habisreuther, F. C. C. Galeazzo, C. Prathap, N. Zarzalis, Structure of laminar premixed flames of methane near the auto-ignition limit, Combust. Flame 160 (12) (2013) 2770–2782.

[69] X. Qin, Y. Ju, Measurements of burning velocities of dimethyl ether and air premixed flames at elevated pressures, Proc. Combust. Inst. 30 (1) (2005) 233–240.

[70] F. N. Egolfopoulos, D. X. Du, C. K. Law, A study on ethanol oxidation kinetics in laminar premixed flames, flow reactors, and shock tubes, Symp. (Int.) Combust. 24 (1) (1992) 833–841.

[71] R. Weber, S. Orsino, A. L. Verlaan, N. Lallemant, Combustion of light and heavy fuel oils in high-temperature air, Journal of the Institute of Energy 74 (499) (2001) 38–47.

[72] G. Pellett, C. Bruno, W. Chinitz, Review of air vitiation effects on scramjet ignition and flameholding combustion processes, in: 38th AIAA/ASME/SAE/ASEE Joint Propulsion Conference & Exhibit, 2002, p. 3880.

[73] H. Pitsch, M. Chen, N. Peters, Unsteady flamelet modeling of turbulent hydrogen-air diffusion flames, Symp. (Int.) Combust. 27 (1) (1998) 1057–1064.

[74] Y. Minamoto, N. Swaminathan, Scalar gradient behaviour in MILD combustion, Combust. Flame 161 (4) (2013) 1063–1075.

[75] O. Desjardins, G. Blanquart, G. Balarac, H. Pitsch, High order conservative finite difference scheme for variable density low Mach number turbulent flows, J. Comput. Phys. 227 (15) (2008) 7125–7159.

[76] G.-S. Jiang, C.-W. Shu, Efficient implementation of weighted ENO schemes, J. Comput. Phys. 126 (1) (1996) 202–228.

[77] M. Germano, U. Piomelli, P. Moin, W. H. Cabot, A dynamic subgrid-scale eddy viscosity model, Physics of Fluids A: Fluid Dynamics 3 (7) (1991) 1760–1765.

[78] C. Meneveau, T. S. Lund, W. H. Cabot, A Lagrangian dynamic subgrid-scale model of turbulence, J. Fluid Mech. 319 (1996) 353–385.

[79] C. D. Pierce, P. Moin, A dynamic model for subgrid-scale variance and dissipation rate of a conserved scalar, Phys. Fluids 10 (12) (1998) 3041.

[80] B. Jochim, M. Korkmaz, H. Pitsch, Scalar dissipation rate based multi-zone model for early-injected and conventional diesel engine combustion, Combust. Flame 175 (2017) 138–154.

[81] N. Peters, Laminar diffusion flamelet models in non-premixed turbulent combustion, Symp. (Int.) Combust. 10 (3) (1984) 319-339.

[82] N. Peters, Laminar flamelet concepts in turbulent combustion, Symp. (Int.) Combust. 21 (1) (1988) 1231-1250.

[83] H. Pitsch, FlameMaster A C++ computer program for 0D combustion and 1D laminar flame calculations. (1998).

[84] E. Mastorakos, Ignition of turbulent non-premixed flames, Prog. Energ. Combust. 35 (1) (2009) 57–97.
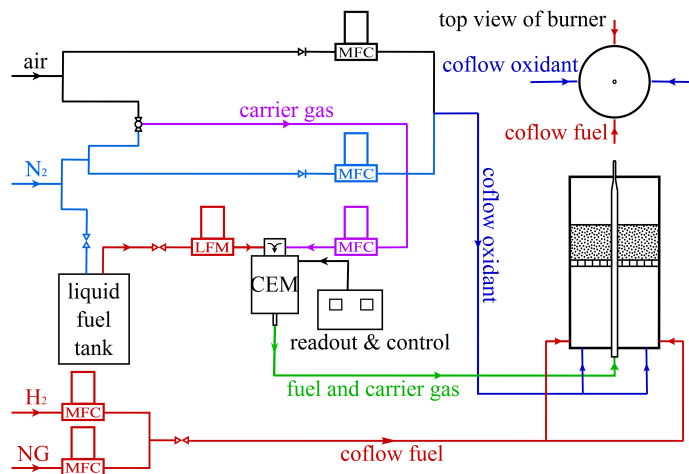
Figure 1: Experimental Setup: CEM is the Controlled Evaporator and Mixer, MFC is the mass flow controller for gases, and LFM is the liquid flow meter.
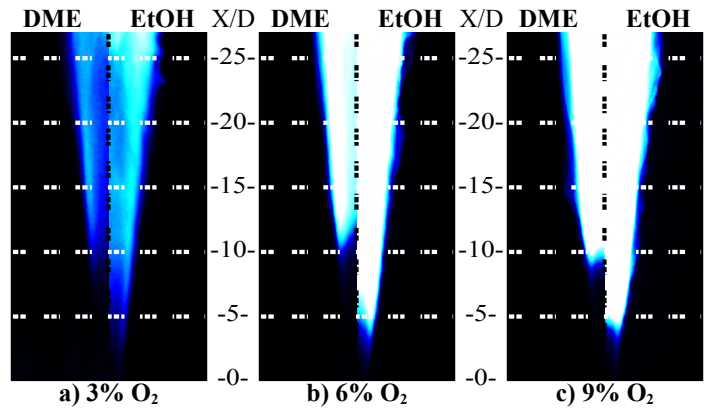
Figure 2: Photographs of DME and ethanol (EtOH) flames carried by nitrogen in the 1250-K coflow with various oxygen concentrations (3%, 6%, and 9% O_2 by volume). The jet flames were shield by the surrounding coflow until approximately $X/D=22$, where X is the axial distance above the jet exit plane and D is the jet diameter.

(a) X/D = 0 - 20

(b) X/D = 3 - 10
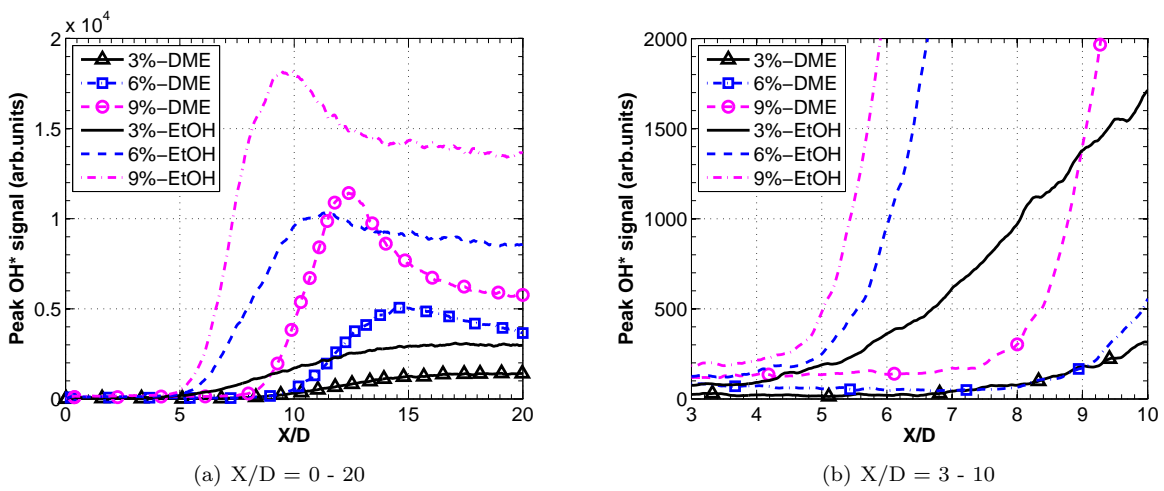
Figure 3: The peak intensity of OH* chemiluminescence at each axial distance in the mean images of ethanol and DME flames carried by N_2
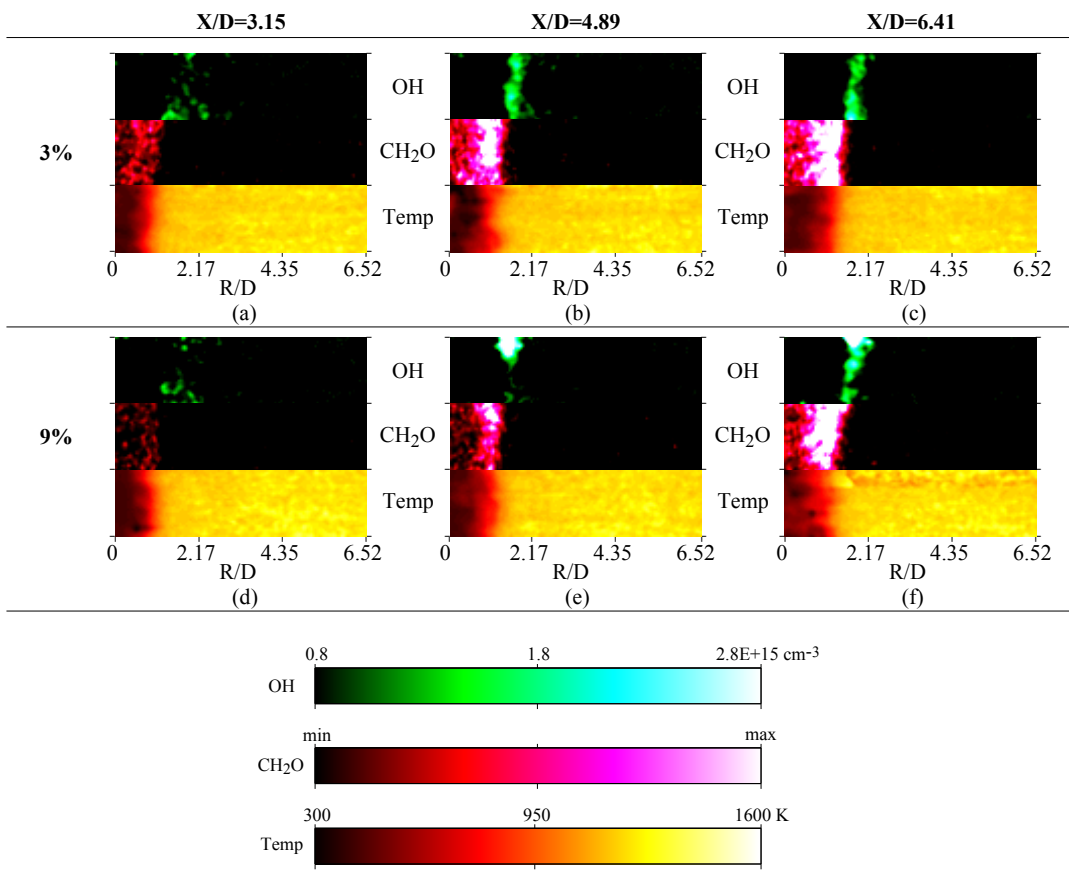
Figure 4: A selection of instantaneous OH (top), CH$_2$O (middle), and temperature (bottom) image triplets for ethanol flames in the 3% and the 9% O$_2$ coflow. These images are centred at X/D = 3.15 (14.5 mm), X/D = 4.89 (22.5 mm), and X/D = 6.41 (29.5 mm) above the jet exit plane, respectively. The left edge of each image is coincident with the jet centreline. Each image 8 × 30 mm.

31

X/D=3.15   X/D=6.41

EtOH

OH
CH$_2$O
Temp

0   2.17   4.35   6.52
R/D
(a)

0   2.17   4.35   6.52
R/D
(b)

DME

OH
CH$_2$O
Temp

0   2.17   4.35   6.52
R/D
(c)

0   2.17   4.35   6.52
R/D
(d)

0.8   1.8   2.8E+15 cm^{-3}
OH

min   max
CH$_2$O

300   950   1600 K
Temp
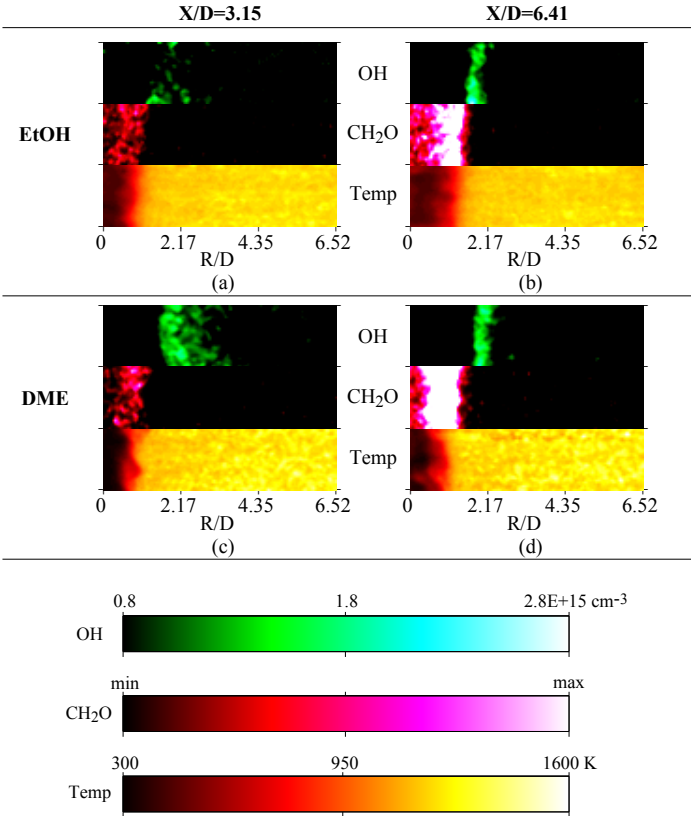
Figure 5: A selection of typical instantaneous OH (top), CH$_2$O (middle), and temperature (bottom) image triplets for ethanol and DME flames in the 3% O$_2$ coflow. These images are centred at X/D = 3.15 (14.5 mm) and X/D = 6.41 (29.5 mm) above the jet exit plane, respectively. The left edge of each image is coincident with the jet centreline. Each image 8 × 30 mm.

X/D=3.15 X/D=6.41

EtOH

OH

CH_2O

Temp

0   2.17   4.35   6.52
R/D
(a)

0   2.17   4.35   6.52
R/D
(b)

DME

OH

CH_2O

Temp

0   2.17   4.35   6.52
R/D
(c)

0   2.17   4.35   6.52
R/D
(d)

0.8   1.8   2.8E+15 cm^{-3}
OH

min   max
CH_2O

300   950   1600 K
Temp
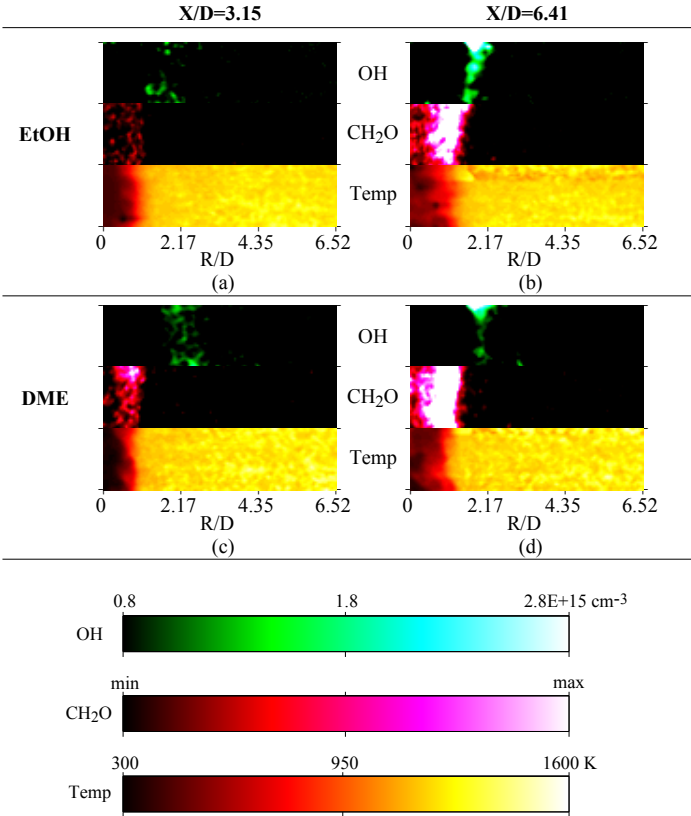
Figure 6: A selection of typical instantaneous OH (top), CH_2O (middle), and temperature (bottom) image triplets for ethanol and DME flames in the 9% O_2 coflow. These images are centred at X/D = 3.15 (14.5 mm) and X/D = 6.41 (29.5 mm) above the jet exit plane, respectively. The left edge of each image is coincident with the jet centreline. Each image 8 × 30 mm.

33
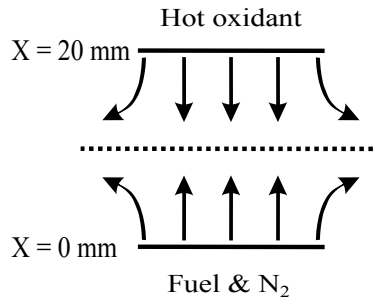
Figure 7: Schematic of the opposed-flow flame setup.

(a) CH$_3$OCH$_3$ decomposition at Z = 0.11

(b) C$_2$H$_5$OH decomposition at Z = 0.15

(c) C$_2$H$_6$ decomposition at Z = 0.07
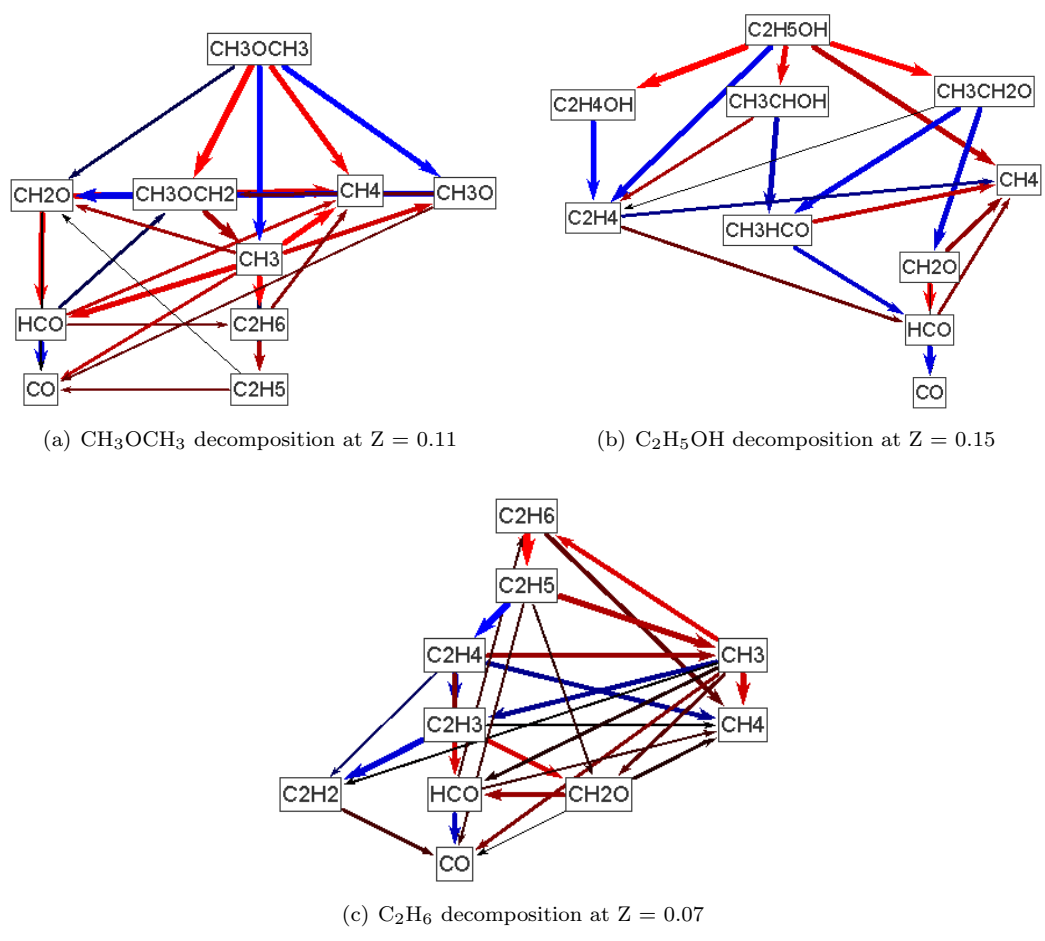
Figure 8: The fuel decomposition pathways at the mixture fraction where the peak fuel consumption rate occurs in the 3% O$_2$ case. The pathways start with the fuel, followed by the nine most important species containing carbon. The thickness of arrows corresponds to the absolute rate of production/destruction. Arrows are coloured by heat, where brown to red indicates the increasing magnitude of positive heat release, and dark to blue indicates the increasing magnitude of negative heat release.
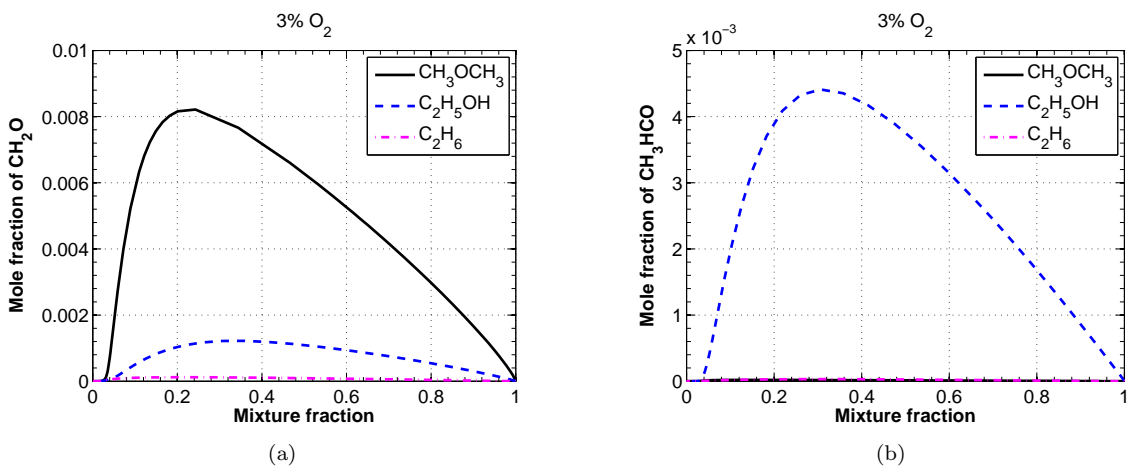
Figure 9: Mole fraction of CH_2O and CH_3HCO as a function of mixture fraction for three fuels with a 3% O_2 hot oxidant.
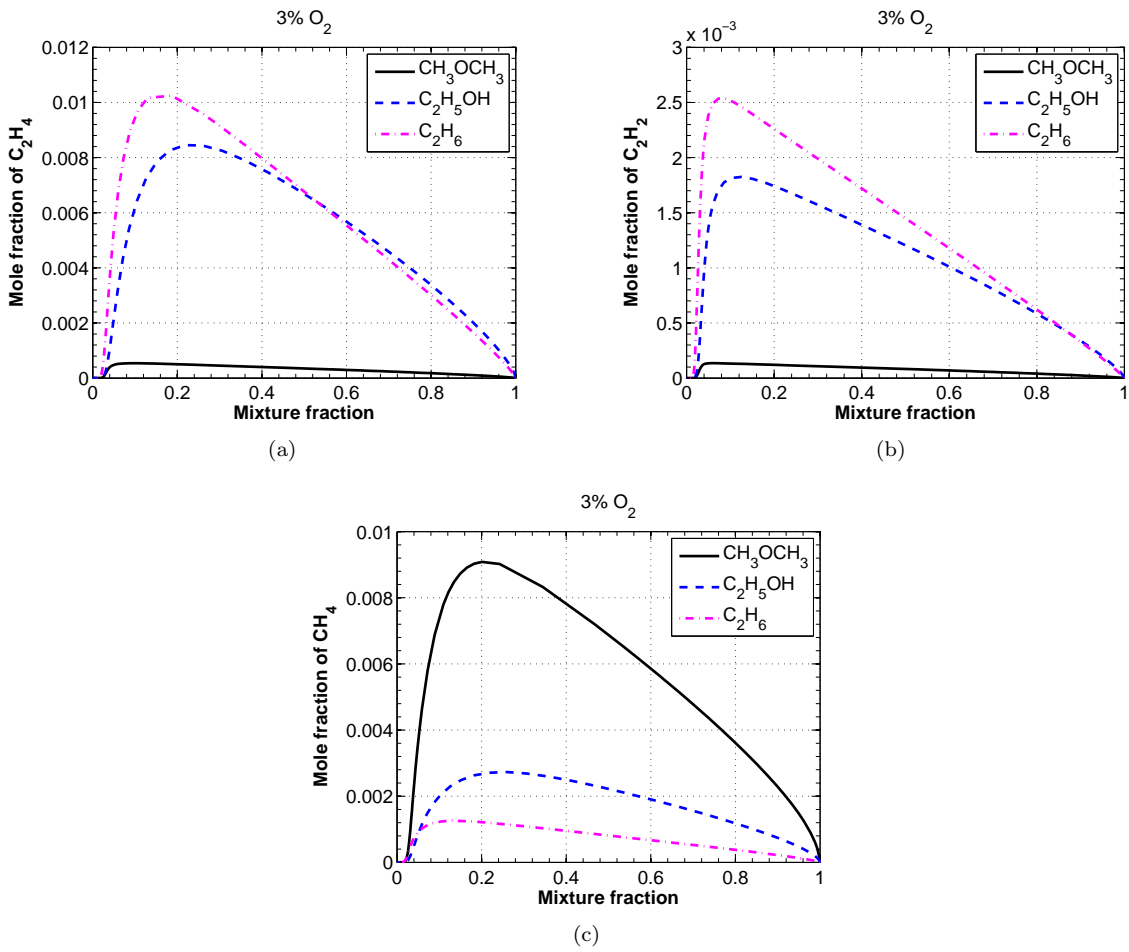
Figure 10: Mole fraction of C_2H_4, C_2H_2, and CH_3 as a function of mixture fraction for three fuels with a 3% O_2 hot oxidant.
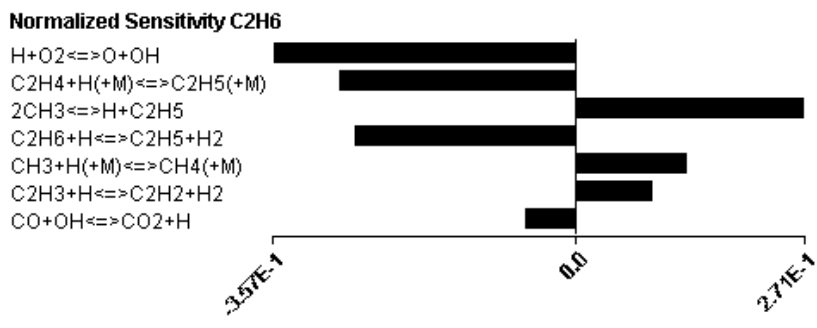
Normalized Sensitivity CH3OCH3

H+O2<=>O+OH
CH3OCH3<=>CH3+CH3O
CH3OCH3+CH3<=>CH3OCH2+CH4
CH3+H(+M)<=>CH4(+M)
2CH3(+M)<=>C2H6(+M)
CO+OH<=>CO2+H
H+O2(+M)<=>HO2(+M)

-1.05E0   0.0   3.36E-1

(a) Sensitivity coefficient of CH_3OCH_3 at Z = 0.11

Normalized Sensitivity C2H5OH

H+O2<=>O+OH
C2H5OH<=>C2H4+H2O
C2H5OH+OH<=>C2H4OH+H2O
C2H5OH+CH3<=>CH3CHOH+CH4
CO+OH<=>CO2+H
C2H5OH+H<=>C2H4OH+H2
2CH3(+M)<=>C2H6(+M)

-1.04E-1   0.0   4.24E-2

(b) Sensitivity coefficient of C_2H_5OH at Z = 0.15

Normalized Sensitivity C2H6

H+O2<=>O+OH
C2H4+H(+M)<=>C2H5(+M)
2CH3<=>H+C2H5
C2H6+H<=>C2H5+H2
CH3+H(+M)<=>CH4(+M)
C2H3+H<=>C2H2+H2
CO+OH<=>CO2+H

-3.57E-1   0.0   2.71E-1
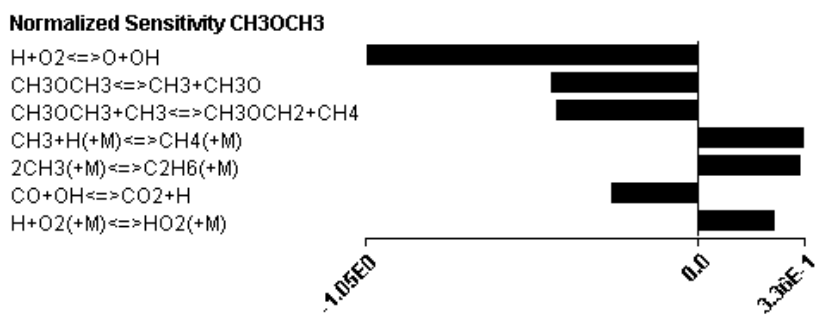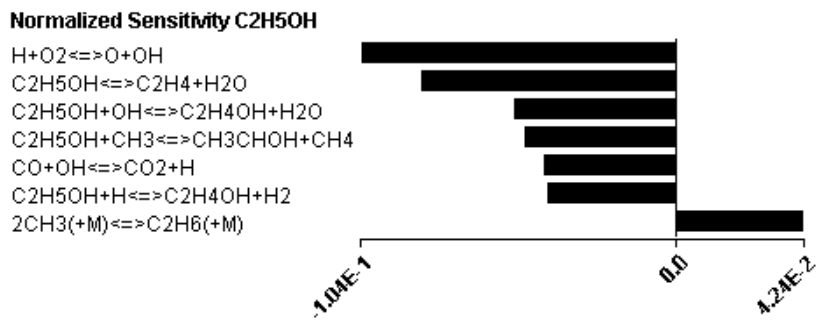
(c) Sensitivity coefficient of C_2H_6 at Z = 0.07

Figure 11: Sensitivity coefficients for the fuel at the mixture fraction where the peak fuel consumption rate occurs for three fuels with a 3% O_2 hot oxidant.

38

(a) CH_3OCH_3

(b) C_2H_5OH

(c) C_2H_6

R1: $H+O_2 \Leftrightarrow O+OH$ R12: $H+OH+M \Leftrightarrow H_2O+M$

R13: $H+OH+M \Leftrightarrow H_2O+M$ R29: $CO+OH \Leftrightarrow CO_2+H$

R52: $CH_3+CH_3(+M) \Leftrightarrow C_2H_6(+M)$ R53: $CH_3+H(+M) \Leftrightarrow CH_4(+M)$

R94: $CH_3+CH_3 \Leftrightarrow H+C_2H_5$ R103: $C_2H_6+H \Leftrightarrow C_2H_5+H_2$

R117: $C_2H_4+H(+M) \Leftrightarrow C_2H_5(+M)$ R126: $C_2H_3+H \Leftrightarrow C_2H_2+H_2$

R239: $CH_3OCH_3 \Leftrightarrow CH_3+CH_3O$
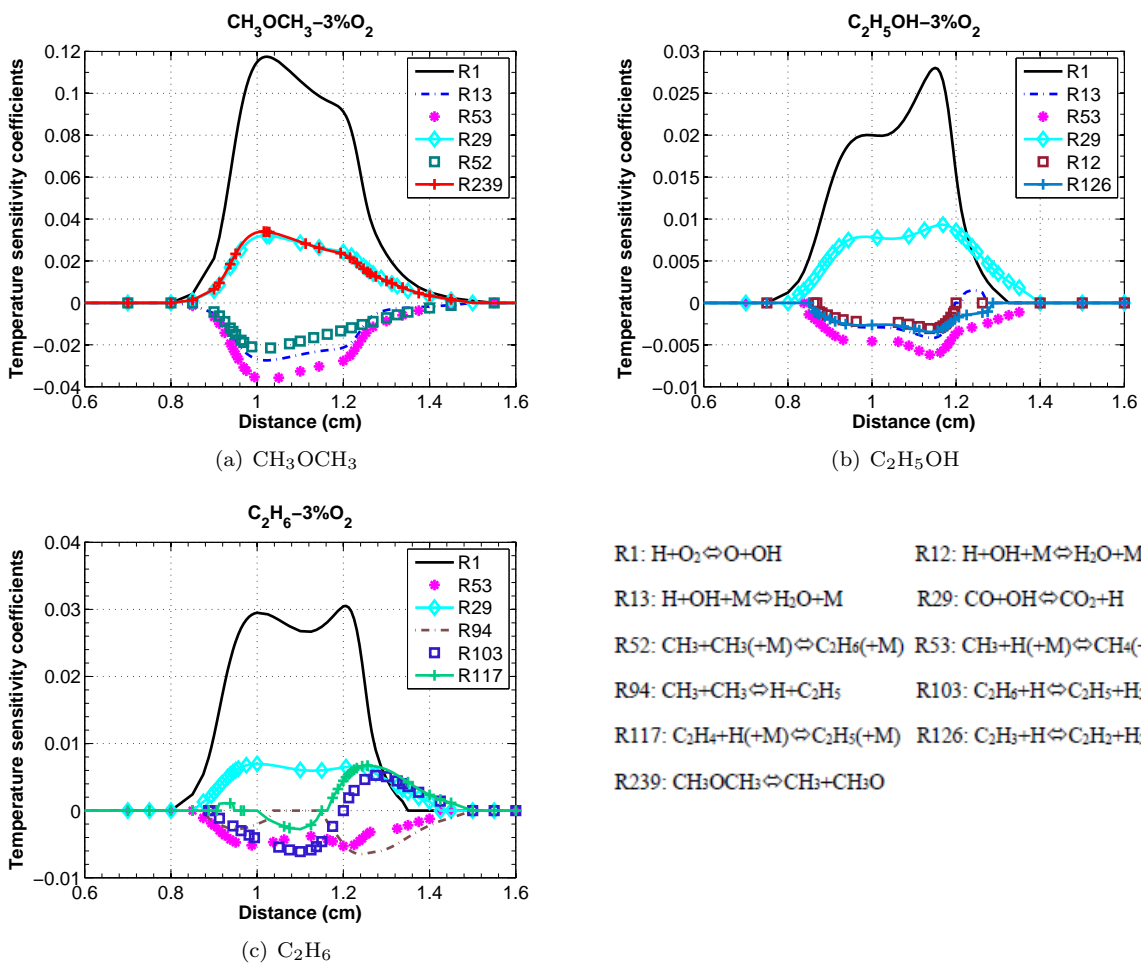
Figure 12: Temperature sensitivity to reaction rates as a function of distance for three fuels with a 3% O_2 hot oxidant.

(a) CH_3OCH_3

(b) C_2H_5OH

(c) C_2H_6
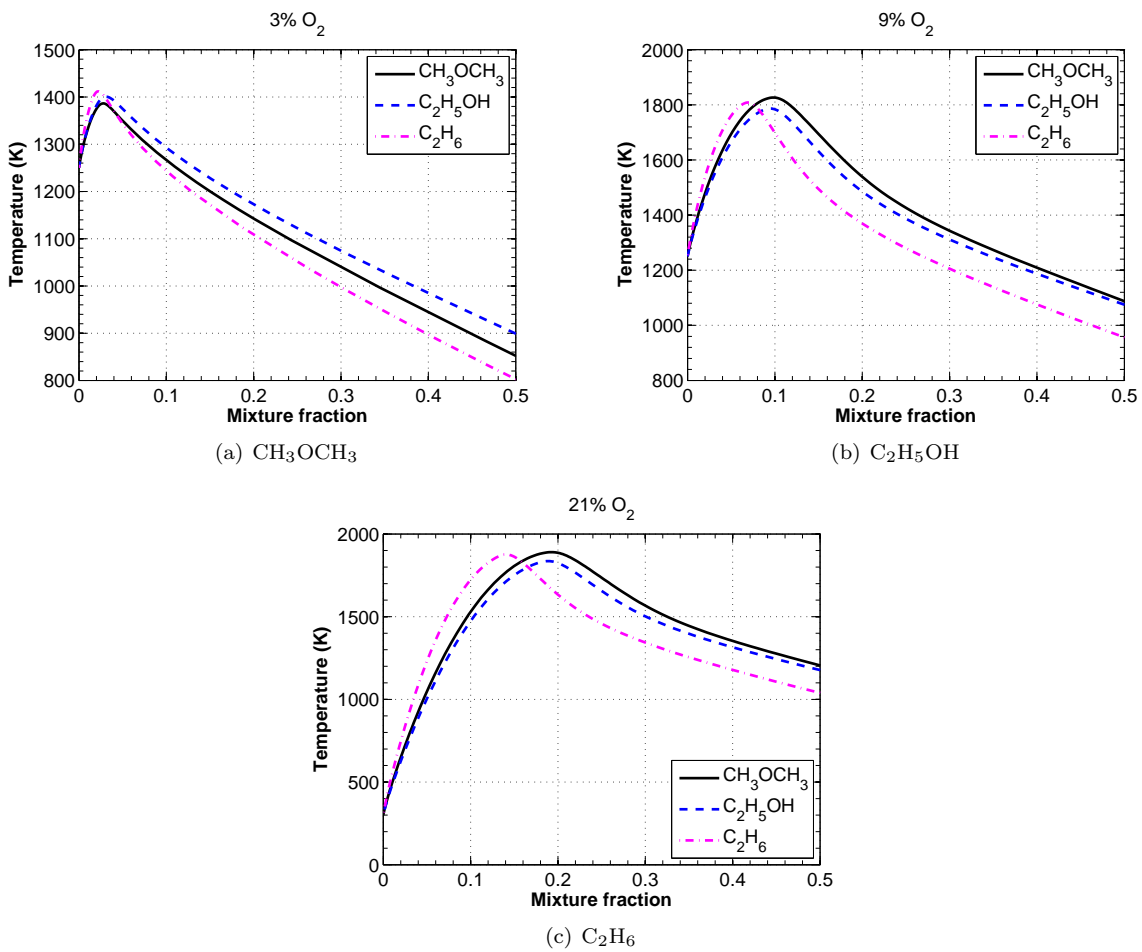
Figure 13: Temperature as a function of mixture fraction for CH_3OCH_3, C_2H_5OH, and C_2H_6 flames burning in a vitiated oxidiser with 3% or 9% O_2 and in a cold air ($O_2 = 21\%$).
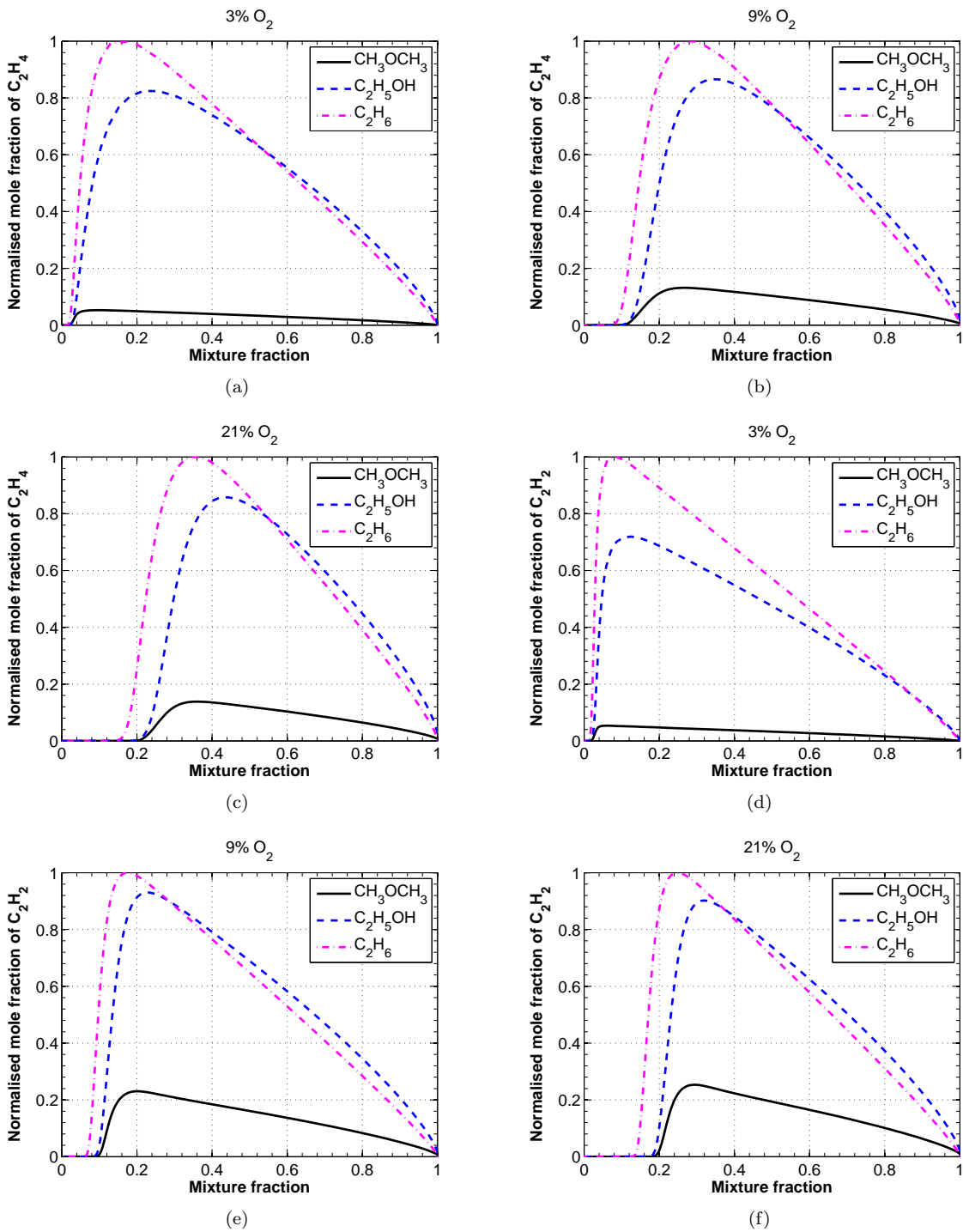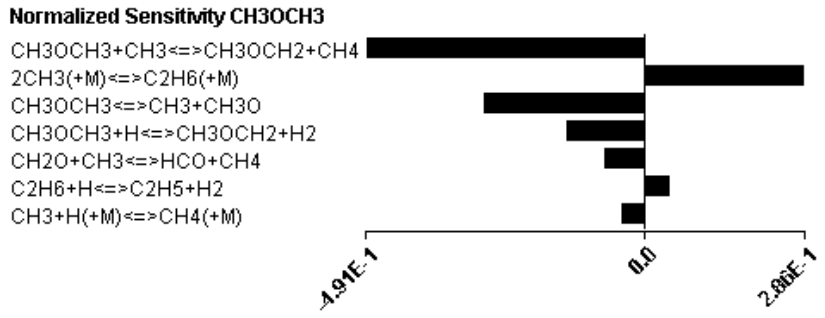
Figure 14: Normalised mole fraction of C_2H_4 and C_2H_2 for CH_3OCH_3, C_2H_5OH, and C_2H_6 flames burning in a vitiated oxidiser with 3% or 9% O_2 and in a cold air ($O_2 = 21\%$). The mole fractions of these species are normalised to their peak mole fractions in the ethane flame at each case.

Normalized Sensitivity CH3OCH3

CH3OCH3+CH3<=>CH3OCH2+CH4
2CH3(+M)<=>C2H6(+M)
CH3OCH3<=>CH3+CH3O
CH3OCH3+H<=>CH3OCH2+H2
CH2O+CH3<=>HCO+CH4
C2H6+H<=>C2H5+H2
CH3+H(+M)<=>CH4(+M)

-4.91E-1   0.0   2.96E-1

(a) Sensitivity coefficient of CH_3OCH_3 at Z = 0.37

Normalized Sensitivity C2H5OH

C2H5OH<=>C2H4+H2O
C2H5OH+H<=>C2H4OH+H2
C2H4+H<=>C2H3+H2
2CH3(+M)<=>C2H6(+M)
CH3CHOH+M<=>CH3HCO+H+M
C2H5OH<=>CH3+CH2OH
C2H5OH+CH3<=>C2H4OH+CH4

-3.07E-1   0.0   1.09E-1

(b) Sensitivity coefficient of C_2H_5OH at Z = 0.33

Normalized Sensitivity C2H6

C2H6+H<=>C2H5+H2
C2H4+H(+M)<=>C2H5(+M)
2CH3<=>H+C2H5
C2H4+H<=>C2H3+H2
C2H3+H<=>C2H2+H2
CH3+H(+M)<=>CH4(+M)
H+OH+M<=>H2O+M

-4.41E-1   0.0   1.54E-1
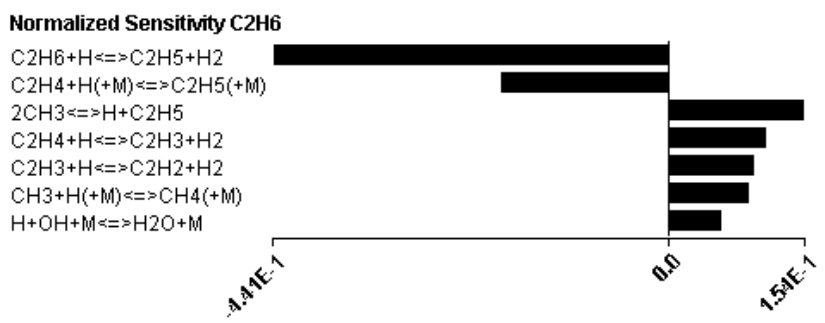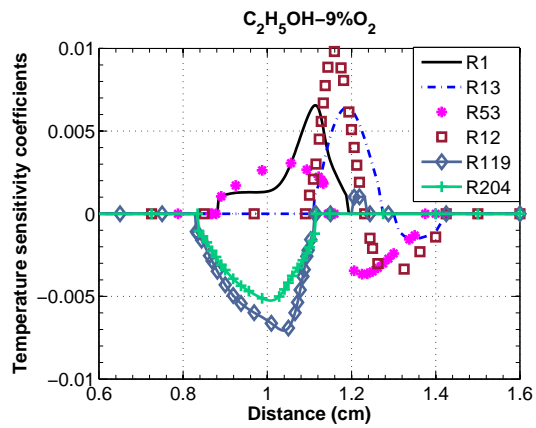
(c) Sensitivity coefficient of C_2H_6 at Z = 0.25

Figure 15: Sensitivity coefficients for the fuel at the mixture fraction where the peak fuel consumption rate occurs for three fuels with cold air as the oxidiser.
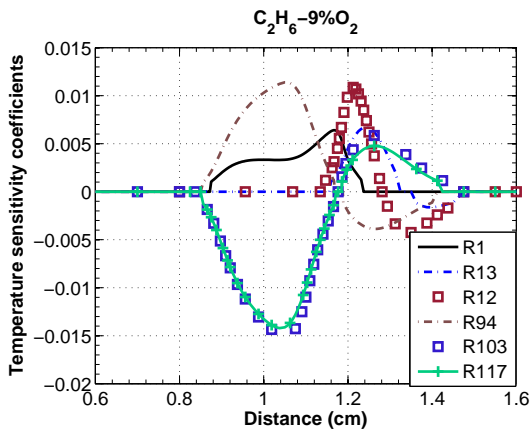
42

(a) CH_3OCH_3

(b) C_2H_5OH

(c) C_2H_6

R1: $H+O_2 \Leftrightarrow O+OH$

R13: $H+OH+M \Leftrightarrow H_2O+M$

R52: $CH_3+CH_3(+M) \Leftrightarrow C_2H_6(+M)$

R94: $CH_3+CH_3 \Leftrightarrow H+C_2H_5$

R117: $C_2H_4+H(+M) \Leftrightarrow C_2H_5(+M)$

R204: $C_2H_5OH \Leftrightarrow C_2H_4+H_2O$

R242: $CH_3OCH_3+CH_3 \Leftrightarrow CH_3OCH_2+CH_4$

R12: $H+OH+M \Leftrightarrow H_2O+M$

R29: $CO+OH \Leftrightarrow CO_2+H$

R53: $CH_3+H(+M) \Leftrightarrow CH_4(+M)$

R103: $C_2H_6+H \Leftrightarrow C_2H_5+H_2$

R119: $C_2H_4+H \Leftrightarrow C_2H_3+H_2$

R239: $CH_3OCH_3 \Leftrightarrow CH_3+CH_3O$
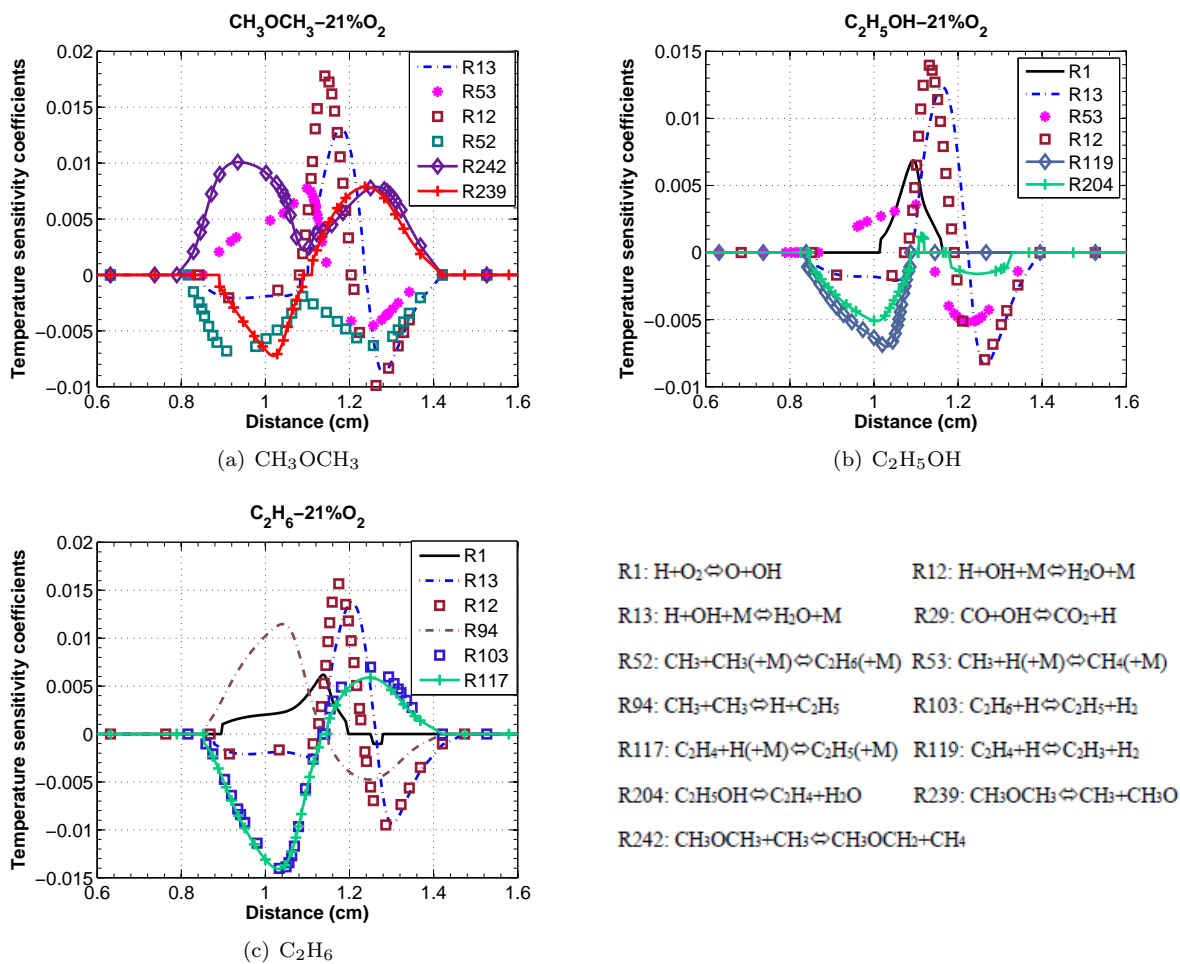
Figure 16: Temperature sensitivity to reaction rates as a function of distance for three fuels with cold air as the oxidiser.

43

Normalized Sensitivity CH3OCH3

CH3OCH3+CH3<=>CH3OCH2+CH4
2CH3(+M)<=>C2H6(+M)
CH3OCH3<=>CH3+CH3O
CH3OCH3+H<=>CH3OCH2+H2
CH2O+CH3<=>HCO+CH4
CH3+H(+M)<=>CH4(+M)
C2H6+H<=>C2H5+H2

-4.84E-1   0.0   2.88E-1

(a) Sensitivity coefficient of CH_3OCH_3 at Z = 0.28

Normalized Sensitivity C2H5OH

C2H5OH<=>C2H4+H2O
C2H4+H<=>C2H3+H2
C2H5OH+H<=>C2H4OH+H2
2CH3(+M)<=>C2H6(+M)
C2H5OH<=>CH3+CH2OH
CH3CHOH+M<=>CH3HCO+H+M
C2H5OH+CH3<=>C2H4OH+CH4

-2.04E-1   0.0   1.03E-1

(b) Sensitivity coefficient of C_2H_5OH at Z = 0.25

Normalized Sensitivity C2H6

C2H6+H<=>C2H5+H2
C2H4+H(+M)<=>C2H5(+M)
C2H4+H<=>C2H3+H2
2CH3<=>H+C2H5
CH3+H(+M)<=>CH4(+M)
C2H3+H<=>C2H2+H2
CH4+H<=>CH3+H2

-3.38E-1   0.0   1.06E-1
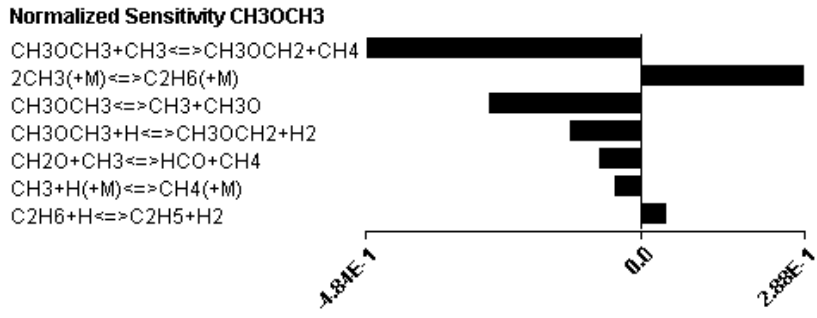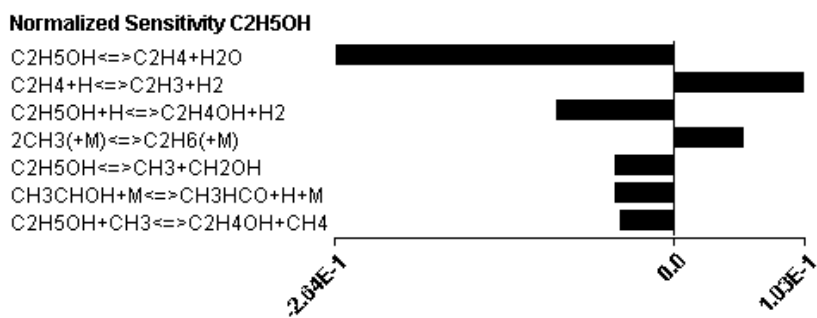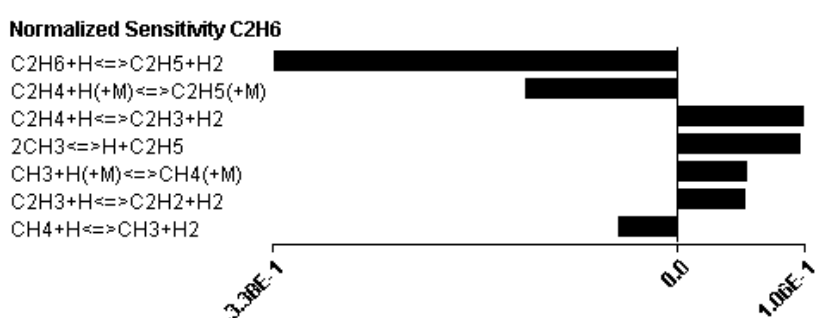
(c) Sensitivity coefficient of C_2H_6 at Z = 0.18

Figure 17: Sensitivity coefficients for the fuel at the mixture fraction where the peak fuel consumption rate occurs for three fuels with a 9% O_2 hot oxidant.

44

(a) CH_3OCH_3

(b) C_2H_5OH

(c) C_2H_6

R1: $H+O_2 \Leftrightarrow O+OH$

R12: $H+OH+M \Leftrightarrow H_2O+M$

R13: $H+OH+M \Leftrightarrow H_2O+M$

R52: $CH_3+CH_3(+M) \Leftrightarrow C_2H_6(+M)$

R53: $CH_3+H(+M) \Leftrightarrow CH_4(+M)$

R94: $CH_3+CH_3 \Leftrightarrow H+C_2H_5$

R103: $C_2H_6+H \Leftrightarrow C_2H_5+H_2$

R117: $C_2H_4+H(+M) \Leftrightarrow C_2H_5(+M)$

R119: $C_2H_4+H \Leftrightarrow C_2H_3+H_2$

R204: $C_2H_5OH \Leftrightarrow C_2H_4+H_2O$

R239: $CH_3OCH_3 \Leftrightarrow CH_3+CH_3O$

R242: $CH_3OCH_3+CH_3 \Leftrightarrow CH_3OCH_2+CH_4$

Figure 18: Temperature sensitivity to reaction rates as a function of distance for three fuels with a 9% O_2 hot oxidant.
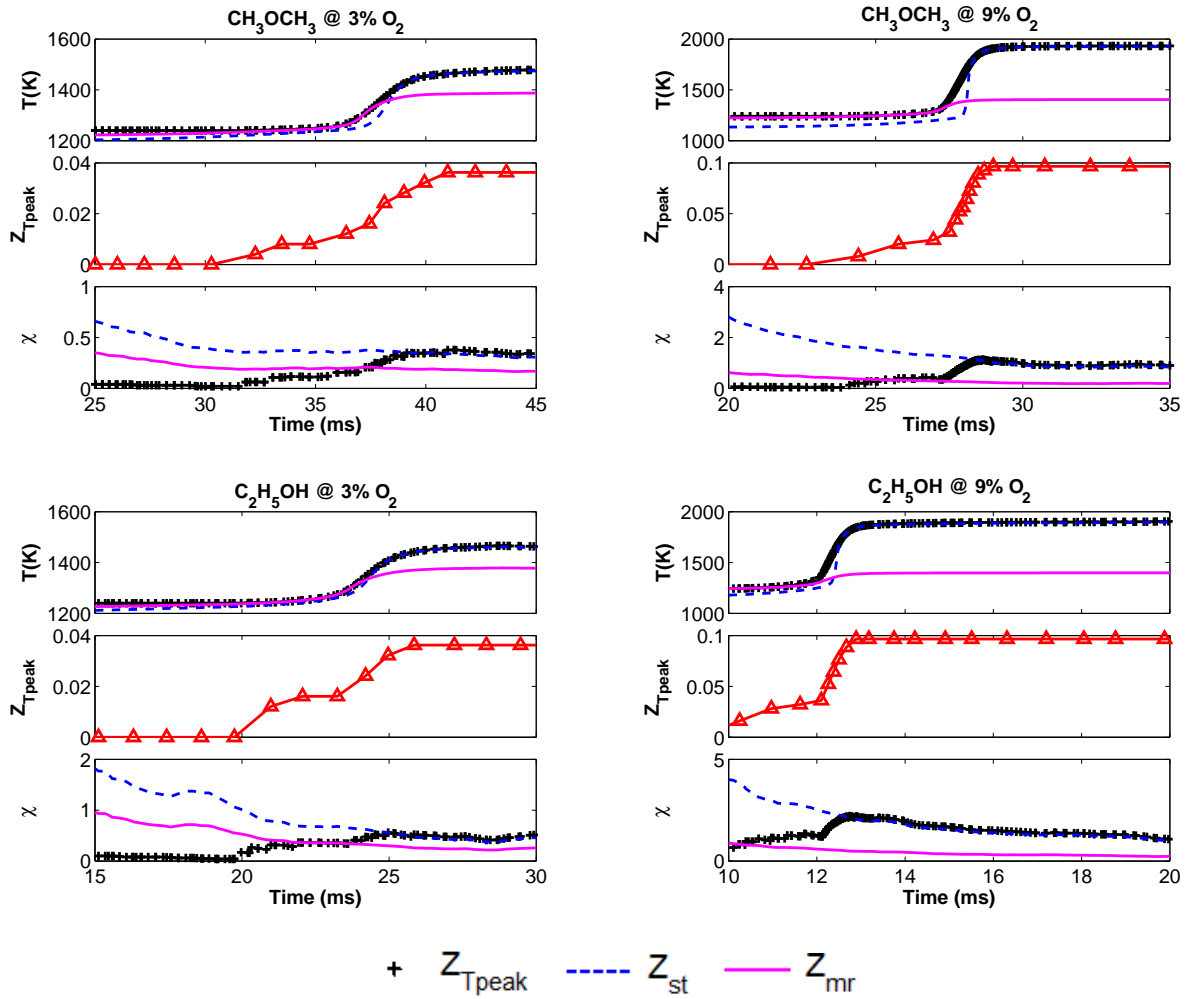
Figure 19: The mixture fraction where the peak temperature occurs is denoted as Z_{Tpeak}. The temperature and the scalar dissipation rate (χ) for ethanol and DME flames at Z_{Tpeak}, Z_{st}, and Z_{mr} in the 3% and 9% O_2 cases are presented as a function of time.
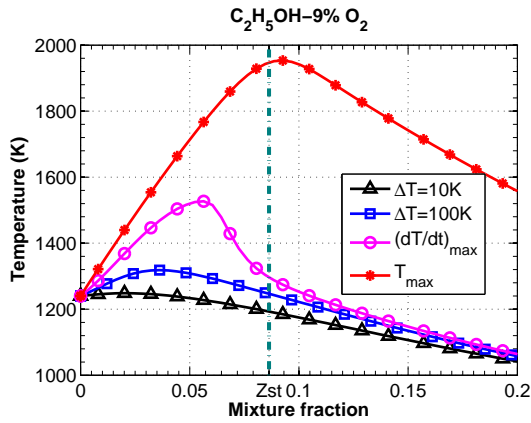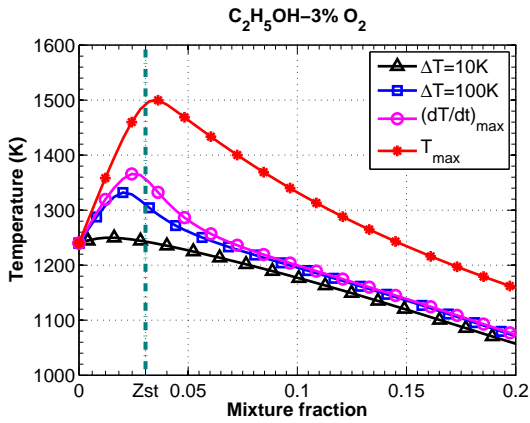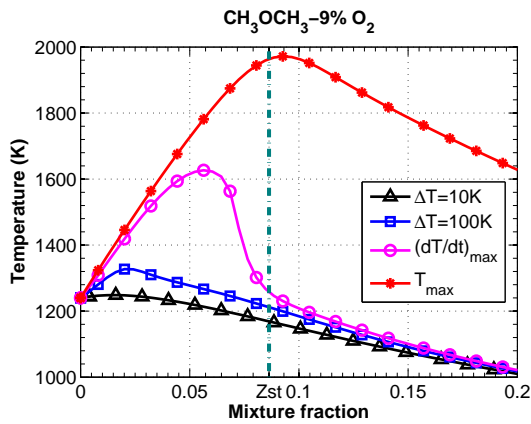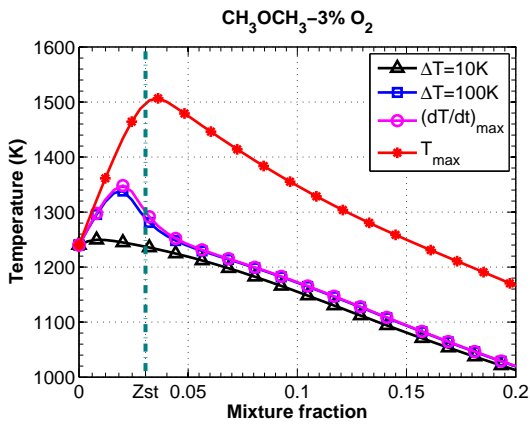
Figure 20: Temperature as a function of mixture fraction at four time steps, including when the temperature increase (ΔT) reaches 10 K, when $\Delta T = 100$ K, when the most rapid change in temperature ($(dT/dt)_{max}$)) occurs, and when the maximum peak temperature occurs.
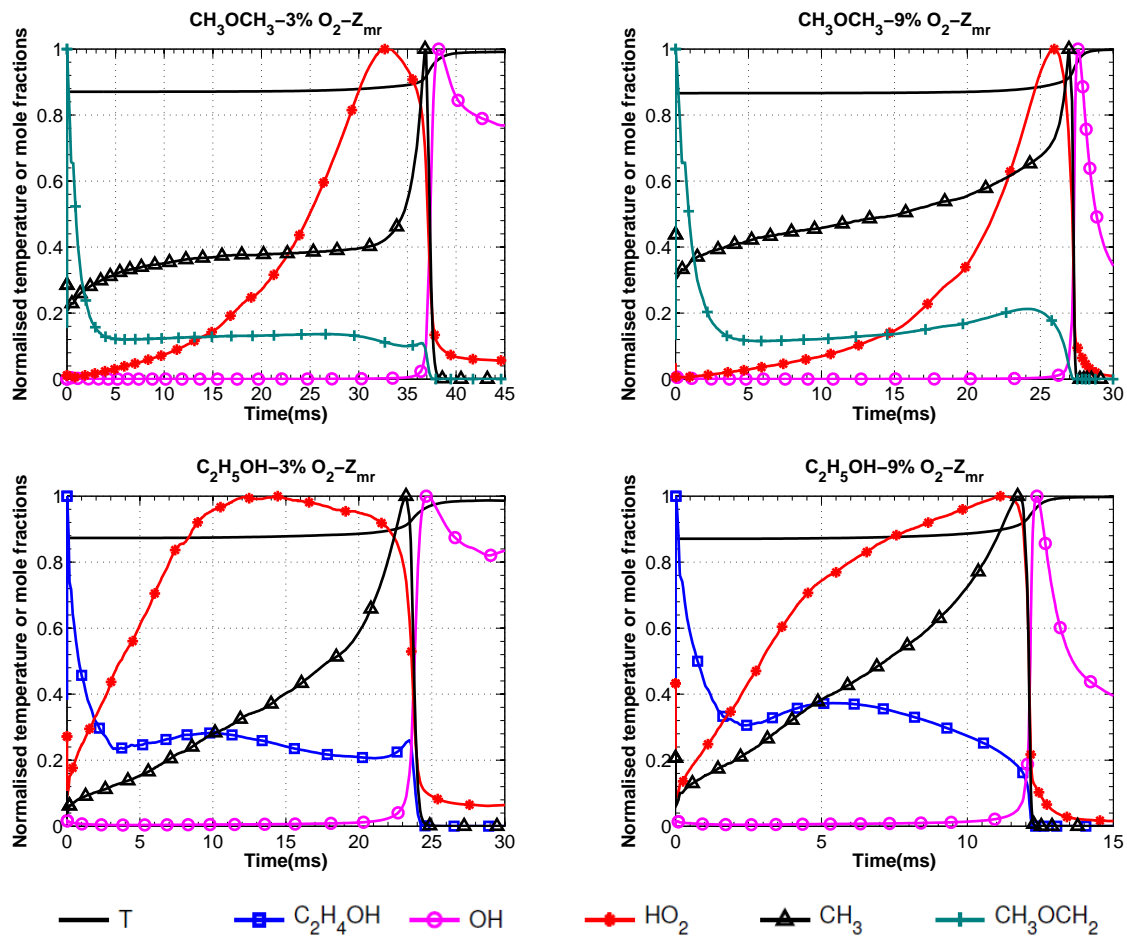
Figure 21: Normalised temperature and mole fractions of some species as a function of time for all cases at the most reactive mixture fraction.

Supplementary Material